Geochemical Modeling of Changes in Shallow Groundwater Chemistry Observed During the MSU-ZERT CO_2 Injection Experiment

[1]*Liange Zheng, [1]John A. Apps, [1]Nicolas Spycher, [1]Jens T. Birkholzer, [2]Yousif K. Kharaka, [2]James Thordsen, [2]Sarah R. Beers, [2]William N. Herkelrath, [2]Evangelos Kakouros, and [3]Robert C. Trautz

[1]Lawrence Berkeley National Laboratory, Berkeley, CA 94720, USA

[2] U.S Geological Survey, Menlo Park, CA 94205, USA

[3] EPRI, Palo Alto, CA 94304, USA

* corresponding author, e-mail: lzheng@lbl.gov

Abstract

A field experiment involving the release of carbon dioxide (CO_2) into a shallow aquifer was conducted near Bozeman, Montana, during the summer of 2008, to investigate the potential for groundwater quality impacts in the case of leakage of CO_2 from deep geological storage. As an essential part of the Montana State University Zero Emission Research and Technology (MSU-ZERT) field program, food-grade CO_2 was injected over a 30 day period into a horizontal perforated pipe a few feet below the water table of a shallow aquifer. The impact of elevated CO_2 concentrations on groundwater quality was investigated by analyzing water samples taken before, during, and following CO_2 injection, from observation wells located in the vicinity of the injection pipe, and from two distant monitoring wells. Field measurements and laboratory analyses showed rapid and systematic changes in pH, alkalinity, and conductance, as well as increases in the aqueous concentrations of naturally occurring major and trace element species.

The geochemical data were evaluated using principal component analysis (PCA) to (1) understand potential correlations between aqueous species, and (2) to identify minerals controlling the chemical composition of the groundwater prior to CO_2 injection. These evaluations were used to assess possible geochemical processes responsible for the observed increases in the concentrations of dissolved constituents, and to simulate these processes using a multicomponent reaction path model. Reasonable agreement between observed and modeled data suggests that (1) calcite dissolution was the primary pH buffer, yielding increased Ca^{+2} concentrations in the groundwater, (2) increases in the concentrations of most major and trace metal cations except Fe could be a result of Ca^{+2}-driven exchange reactions, (3) the release of anions from adsorption sites due to competitive adsorption of carbonate could explain the observed trends of most anions, and (4) the dissolution of reactive Fe minerals (presumed

ferrihydrite and fougerite, from thermodynamic analyses) could explain increases in total Fe concentration.

1. Introduction

The capture of CO_2 and its storage in deep subsurface reservoirs is one of the options currently being considered to mitigate rising anthropogenic greenhouse gas concentrations in the atmosphere (Bachu, 2000; White et al., 2005). The proper site selection and management of CO_2 storage reservoirs is expected to minimize the risks to human health and the environment. However, the possibility of CO_2 leakage cannot be completely ruled out, in which case the stored CO_2 could migrate following preferential pathways upward into overlying shallow groundwater resources. The dissolution of CO_2 into a freshwater aquifer would increase its acidity (from carbonic acid), which in turn could increase the dissolved concentrations of trace elements potentially present in aquifer materials and detrimentally impact groundwater quality. Therefore, the potential impact of CO_2 intrusion on the quality of fresh water aquifers overlying CO_2 storage sites needs to be investigated.

The increase in the concentration of trace elements is expected to be the main potential deleterious effect on potable groundwater. The pH decrease by itself could also be counted as a detrimental effect to water quality, although carbonic acid is a weak acid that is expected to be significantly buffered by aquifer minerals. The mobilization of trace metals by supercritical CO_2 in deep CO_2 storage reservoirs has been previously evidenced. For example, Kharaka et al. (2009) reported a temporary rise in the dissolved concentrations of Fe and other various metals after CO_2 injection at the Frio test site. Carroll (2009) also reported increases in concentrations of various cations in batch experiments when aquifer rocks were exposed to wet supercritical CO_2 under the temperature and pressure conditions of a deep CO_2 storage reservoir.

Investigations on the mobilization of trace elements in response to CO_2 intrusion into potable groundwater are relatively recent. Laboratory experiments (McGrath et al., 2007; Smyth et al., 2009; Lu et al., 2010; Little and Jackson, 2010), usually involving the release of CO_2 into a pre-equilibrated water-rock environment, have been conducted to investigate this issue. McGrath et al. (2007) reported an increase in cadmium concentrations in a batch experiment in which CO_2 gas was equilibrated with sediments and ground water from uncontaminated aquifers. Smyth et al. (2009) observed rapid increases in concentrations of some cations (Ba, Ca, Fe, Mn and Sr) in laboratory batch experiments of various aquifer materials exposed to CO_2. Lu et al. (2010) conducted laboratory batch experiments to explore the impact of CO_2 on groundwater quality using a series of aquifers materials from the Texas Gulf Coast region. Two different types of responses were observed in this study: "Type I cations" (Ca, Mg, Si, K, Sr, Mn, Ba, Co, B, Zn) displayed rapidly increasing concentrations at the start of CO_2 injection that became steady before the end of the experiment, whereas "Type II cations" (Fe, Al, Mo, U, V, As, Cr, Cs, Rb, Ni and Cu) showed initial concentration increase at the start of CO_2 injection followed by a decrease to values lower than levels prior to injection. Little and Jackson (2010) performed laboratory incubations of CO_2 infiltration for more than 300 days on samples from different freshwater aquifers. While increases in the concentration of alkali and alkaline earth metals were quite consistent in most of their samples, increases in trace element concentrations were only observed in some samples.

Laboratory experiments, on the one hand, provide useful insight into the potential impact of CO_2 on groundwater; on the other hand, they have important limitations. For example, the water-rock environment prior to the release of CO_2 might not be properly represented because the pre-equilibration of a synthetic solution (e.g., Smyth et al., 2009) or DI water (Lu et al., 2010)

with sediments usually creates a water-rock environment different from *in situ* conditions. Unwanted oxidation during the experiment (e.g., Little and Jackson, 2010) might also dampen the effect of CO_2 on the reaction of some redox sensitive elements. Moreover, to our knowledge, most if not all of the current laboratory studies have been conducted in batch reactors, without considering the transport of groundwater and CO_2.

The mobilization of trace metals has also been reported in several groundwater systems exposed to natural sources of CO_2 (e.g., Aiuppa et al. 2005; Flaathen et al. 2009; Keating et al., 2010; Arnorsson et al., 2010). Investigating volcanic aquifers near Mount Vesuvius in Italy, Aiuppa et al. (2005) indicated increasing concentrations of most trace elements with increasing bicarbonate concentrations. Arnorsson et al. (2010) suggested that CO_2-rich waters from a basaltic aquifer in Iceland are higher in Ca, Mg, Fe and many trace elements. Keating et al. (2010) reported contrasting results for a natural analog in New Mexico, USA, where the pH depression and consequent trace element mobility were relatively minimal due to the buffering capacity of the aquifer, despite relatively high levels of dissolved CO_2. In addition to the variability in the geological and geochemical conditions of these aquifers, one possible reason for these different observations is the reversibility of the chemical reactions induced by the CO_2. For example, as discussed by Flaathen et al. (2009), toxic metals that are initially liberated by the dissolution of basalt reacting with acidic CO_2-rich solutions may be reincorporated into solid phases as the groundwaters are neutralized by continued basalt dissolution. Another possibility may be the precipitation of metals upon CO_2 degassing (during sampling or during fluid ascension to shallower depths), as recognized long ago in the case of CO_2-ladden hydrothermal waters (e.g., Drummond and Omohto, 1985; Spycher and Reed 1989).

Numerical models have also been used to evaluate CO_2-related aqueous reactions (Wang and Jaffe, 2004; Carroll et al., 2009; Zheng et al., 2009; Apps et al., 2010; Wilkin and Digiulio, 2010). Wang and Jaffe (2004) conducted reactive transport simulations for CO_2 leakage into a generic aquifer containing the lead-bearing mineral galena. While highlighting the need for further research, their results are not necessarily representative of a realistic case because of their simplified conceptual model representing extreme conditions (i.e., supercritical CO_2 reacting with large amounts of galena). Carroll et al. (2009) conducted reactive transport simulations to evaluate the pH and alkalinity response to a hypothetical CO_2 intrusion case in the High Plains aquifer in the central United States. While useful for understanding CO_2-induced pH variations and evaluate options for monitoring CO_2 leakage, the issue of trace metal release was not directly addressed. Reactive transport simulations conducted by Zheng et al. (2009) and Apps et al. (2010) suggested that elevated levels of CO_2 in groundwater could give rise to significant increases in aqueous lead and arsenic concentrations.

Numerical models of water-CO_2-rock interaction in deep storage formations (e.g., Kharaka et al., 2006, 2009; Knauss et al., 2005; Xu et al. 2004; 2005; Zerai et al., 2006) provide additional information on the possible chemical reactions that could occur when CO_2 leaks into shallow aquifers, although the results of such models have to be examined cautiously considering the considerably higher CO_2 pressures, and to a lesser extent higher temperatures, at the depth of deep storage reservoirs compared to conditions in typical drinking water aquifers. The chemical processes potentially responsible for the mobilization of trace elements include the dissolution of carbonates (e.g., Kharakha et al., 2006; McGrath et al., 2007; Birkholzer et al., 2008), sulfides (e.g., Wang and Jaffe, 2004; Zheng et al., 2009; Apps et al., 2010) and iron oxyhydroxide minerals (e.g., Kharaka et al., 2006, 2009), as well as surface reactions such as adsorption/de-

sorption and ion exchange (Kharaka et al., 2006, 2009; Zheng et al., 2009; Apps et al., 2010). The reaction path and kinetic model study conducted by Wilkin and Digiulio (2010) further indicates that the geochemical response of an aquifer to CO_2 leakage is closely related the aquifer mineralogy.

On the basis of these previous investigations, it is thus expected that differences in geology, mineralogy, and groundwater chemistry at any particular site could all lead to different responses to CO_2 leakage. For this reason, as noted by Apps et al. (2010), field tests integrated with modeling studies are necessary to further assess hydrogeochemical processes potentially affecting groundwater quality upon a CO_2 release. The CO_2 leakage test at the Montana State University Zero Emission Research and Technology (MSU-ZERT) field site, located at Bozeman, Montana, provided such an opportunity. In the summer of 2008, CO_2 was injected into a shallow aquifer (Spangler et al., 2010) to evaluate atmospheric and near-surface detection techniques relating to the potential leakage of CO_2. Although not the primary purpose of the field test, the controlled-release test permitted study of the impact of elevated CO_2 levels on groundwater quality through analysis of water samples taken before, during and following CO_2 injection (Kharaka et al., 2010). In this paper, we describe the interpretation of the geochemical data via statistical analyses, evaluation of thermodynamic controls, and geochemical modeling. Our main objectives were to explore the potential geochemical processes relating to CO_2 contamination of subsurface potable water sources, and to refine sampling and analytical protocols necessary for future targeted field investigations.

In the following sections, we provide a brief description of the ZERT field test and discuss some pertinent issues relating to our evaluation and interpretation of chemical analyses from the collected groundwater samples. We provide a statistical evaluation of the geochemical

data to identify possible geochemical processes that might have affected the observed changes in the concentrations of various major and trace element species in solution, followed by a thermodynamic evaluation of the factors governing the composition of the groundwaters prior to CO_2 injection. In particular, we examine factors potentially affecting the redox state of the system. Finally, we use the results of these geochemical investigations to set up a numerical model to simulate the observed geochemical response to CO_2 leakage. The model results are then compared with the field observations. We conclude with a discussion of the results, provide recommendations regarding future field tests, and finally highlight remaining uncertainties relating to the present modeling.

2. The MSU-ZERT field test

The ZERT field site is located at the western edge of the Montana State University (MSU) Bozeman campus on a flat piece of agricultural land (Spangler et al., 2010). Details regarding the regional setting, test methods, as well as hydrogeological and geochemical conditions of the test area are given in Spangler et al. (2010) and Kharaka et al. (2010). The maximum water level fluctuation was 0.28 m during the test (Figure 2 in Kharaka et al., 2010). The CO_2 injection test was conducted in a shallow water-table aquifer with water levels fluctuating around 1 m below ground surface (Figure 1). Gaseous CO_2 was injected approximately 0.75 m below the water table through a 70 m long horizontal perforated pipe placed approximately perpendicular to the regional hydraulic gradient. Approximately 300 kg/day of food-grade CO_2 was injected between July 9 and August 7, 2008. As part of the project, United States Geological Survey (USGS) staff collected groundwater samples at five locations (Figure 2) about 1–6 m from the injection pipe before, during and following CO_2 injection (Kharaka et al., 2010). Two observation wells were

installed at each location, one screened at 3 m (10 feet) (referred to as A wells) and the other at 1.5 m (5 feet) (referred to as B wells) below ground (a total of 10 observation wells). Headspace gas samples were also taken from the wells for analysis, and several *in situ* Eh measurements were made. Over 60 groundwater samples were subsequently analyzed for thirty chemical constituents including major ions and trace metals, temperature, electrical conductance (EC), pH, alkalinity, and calculated total dissolved solids (TDS) (Kharaka et al., 2010).

The geologic section at the test site consists predominantly of a thin unsaturated layer of mostly sandy silt (see Figure 3 left) underlain by saturated coarse sand, gravel and and cobbles (see Figure 3 right) with high permeability (0.76-1.4 m/d), yielding fast groundwater seepage velocities around 2 m/d (Kharaka et al., 2010). Ambats et al. (2009) describe the mineralogical analyses of cored sections to a depth of approximately 3 m. Sediments in the saturated zone are composed predominantly of a matrix of rounded cobble-sized fragments, consisting primarily of andesitic volcanic rocks with predominant plagioclase, quartz-biotite-amphibole gneiss, and red granite. The mafic volcanic rock fragments are strongly magnetic, likely due to the presence of magnetite. Minor limestone and occasional dolomite fragments are also observed in the matrix. Unspecified Fe oxides appear in the <0.25 mm fraction as "powdery orange blebs." Secondary carbonate coatings are found throughout the core, and a caliche zone is present in the zone overlying the water table about one meter below the land surface. Small quantities of clay (≈ 1 wt%), consisting mainly of smectite and minor kaolinite, are also found in the saturated zone.

Analyses reported by Kharaka et al. (2010) indicate that groundwater at the site is of calcium-bicarbonate type, moderately dilute (TDS ~ 600 mg/L), and with a pH value of approximately 7.0. Typical background calcium and bicarbonate concentrations are around 90 and 400 mg/L, respectively, whereas chloride and sulfate concentrations remain below 10 mg/L.

The baseline concentrations of trace metals are very low, typically in the range of 10–20 µg/L for B and Cr, 1–10 µg/L for Al, As, Cu, Li, Se, U and Zn, and below 1 µg/L for Mo, Co, Cd, and Pb.

During CO_2 injection, TDS levels increased to values of up to 1500 mg/L, mostly as a result of CO_2 dissolution in water (bicarbonate concentrations increased up to about 1200 mg/L) and a significant increase in calcium (~ up to 240 mg/L) presumably from the dissolution of calcite. The pH decreased to values between 5.5 and 6, and the concentration of alkali earth metals increased by a factor of 2 to 5. The concentrations of most trace metals showed a smaller but systematic increase, although none exceeded the maximum contaminant levels (MCL's) adopted by the U.S. Environmental Protection Agency (EPA).

3. CO_2 migration upon injection

The transport of CO_2 in the subsurface at the ZERT site has been assessed in other studies (Lewicki et al., 2007; Strazisar et al., 2009; Oldenburg et al., 2010). Groundwater flow velocities may be as high as 3.8 m/d (Kharaka et al., 2010), and rates of CO_2 transport in the unsaturated zone are estimated to be an order of magnitude higher. CO_2 concentrations in gas samples obtained from the head space of wells 1B, 2B, and 5B increased up to about 90% (by volume) only two days after injection started (Strazisar et al., 2009), confirming that CO_2 transport in the unsaturated zone was very fast. Model results from Oldenburg et al. (2010) also indicate that gaseous CO_2 spreads out fast through the vadose zone under the soil layer. It is thus quite certain that dissolution of gaseous CO_2 back into groundwater was a prominent process triggering the chemical changes measured in the groundwater samples. Based on results from a recent tracer test reported by Thordsen (2011), the transport of dissolved CO_2 with the fast groundwater flow is an additional process leading to elevated CO_2 concentrations and water quality changes at monitoring locations, at least in the shallower wells located downstream from the injection pipe.

It should be noted that groundwater in the deeper A-wells was essentially not impacted by either aqueous or gaseous CO_2 transport. Redissolution of gaseous CO_2 was limited to a small layer at the soil-groundwater interface, while the flow of CO_2-charged water from the injection well bypassed the A-wells because their screen interval is too deep (Figure 1).

Because uncertainties remain regarding the gas and groundwater flow rates, recharge effects, and subsurface heterogeneity, no attempts were made in this study to model the multi-phase reactive transport processes of CO_2 and water in the subsurface. We focus instead solely on geochemical "batch" modeling of reactive processes (i.e., chemical reactions upon increasing CO_2 levels without transport), such that the transport specifics responsible for increased CO_2 levels at monitored locations do not need to be modeled.

4. Geochemical interpretation of groundwater analyses

Several steps were undertaken to qualitatively interpret chemical analyses of samples taken from the ZERT site, in an effort to provide a framework for the geochemical modeling conducted in Section 5.

4.1. Data selection

Rapid and systematic changes following CO_2 injection were observed in the chemical parameters measured at the site. However, these trends were interrupted by periodic precipitation events, which caused immediate fluctuations in the water table and perturbed the groundwater chemistry in ways that could not be attributed to CO_2 injection (Kharaka et al., 2010). To avoid the complexities introduced by random rainfall events, we restricted our geochemical evaluation to 21 complete analyses of groundwater samples taken during the period utilized to establish the baseline ambient chemistry of the groundwater (July 7 to 8, 2008) and the period between the

start of CO_2 injection and the occurrence of the first significant rainfall event (July 17, 2008). Although of limited duration, this time period allows evaluation of the short-term response of groundwater chemistry to the injection of CO_2. Because of the broad similarities in the chemical responses of the samples, regardless of well location (Kharaka et al., 2010), the chemical analyses from all wells were utilized for this study.

4.2. Thermodynamic evaluation of initial groundwater composition

Identification of potential thermodynamic and kinetic controls influencing the chemical composition of the groundwater before the release of CO_2 can help explain the subsequent behavior resulting from increasing partial pressure of CO_2 ($P(CO_2)$). Seven samples taken from various monitoring wells immediately prior to CO_2 injection were available for evaluation. The concentrations of species in these seven samples were generally comparable except for the anomalously high concentrations of Fe, Cu, Cd, Cr and Mo in two samples, which were discarded as outliers, possibly resulting from mineralogical heterogeneity. Average values for the remaining five samples were therefore calculated, as shown in Table 1.

By calculating saturation indices, a thermodynamic analysis is used to evaluate whether the primary and secondary minerals comprising the aquifer sediments might exercise thermodynamic control over the chemical composition of the groundwater. Our analysis included both redox-sensitive (e.g. ferrihydrite) and redox-insensitive (e.g. calcite) minerals. Because the redox state in the aquifer was unlikely to be in thermodynamic equilibrium, the variation in the saturation indices of redox-sensitive minerals was explored by varying the redox state over a wide range from pe = -4 to +16 for the given initial chemical composition, pH and temperature of the groundwater. Upon lowering pe, almost all of the trace metals of interest could precipitate in very low solubility host minerals, due to the trace element or a co-component

being directly affected by a change in redox state. The trace elements As, Cr, Co, Cu, Mo, Se and U could be affected directly, whereas Cd, Pb and Zn could be indirectly affected through precipitation as selenides and sulfides. The aqueous concentrations of other elements such as C, Fe, Mn, N and S could also be impacted by the redox state. Only Ba would remain essentially unaffected.

The analysis suggests that the initial groundwater composition at ZERT was controlled mainly by the products of the weathering of primary minerals composing the detrital rock fragments of the sediment framework. Such weathering products may be unstable or metastable, for example hydroxy-aluminum silicates such as imogolite ($Al_2SiO_5.xH_2O$), opal-CT (SiO_2), ferrihydrite ($Fe(OH)_3$), and fougerite ($[2/9Fe^{II}(OH)_2.1/3Fe^{III}(OH)_2.4/9Mg(OH)_2]^{+1/3}[1/3A]^{-1/3}$; A = ($2/3HCO_3^-.1/6CO_3^{-2}$) (also known as "green rust"). Others, such as calcite ($CaCO_3$), barite ($BaSO_4$) and crandallite ($CaAl_3(PO_4)(OH)_5.H_2O$) are typically more stable. Geochemical modeling indicates that the groundwater is undersaturated with respect to most of these minerals (Table 2). This may be the result of dilution (by a factor of about two) resulting from approximately five inches of rainfall during the two months preceding sampling. Of the secondary phyllosilicates identified in the sediment matrix, smectite ($Ca_{0.145}Mg_{0.26}Al_{1.77}Si_{3.97}O_{10}(OH)_2$), kaolinite ($Al_2Si_2O_5(OH)_4$), and illite ($K_{0.6}Mg_{0.25}Al_{1.8}Al_{0.5}Si_{3.5}O_{10}(OH)_2$) were all significantly supersaturated, the supersaturation being imposed by the slow rates of crystallization of these minerals under the prevailing conditions and/or too high Al concentrations reflecting colloidal Al in addition to truly dissolved Al (which is not uncommon, e.g. Lindsay and Walthall, 1996).

There are indications that many of the redox-sensitive trace element concentrations might be controlled by the precipitation of either reduced oxides, elements, or selenides, consistent with

reductive processes operating through the biogenic oxidation of organic matter, and broadly consistent with measured *in situ* redox potentials ranging from pe = +1.5 to pe = +2.5 (Kharaka et al., 2010). In contrast, the presence of NO_3, the very low concentrations of total Fe and total Mn, and the predicted co-saturation of fougerite and ferrihydrite at pe ≈ +9 suggests somewhat more oxidizing conditions, which might have been buffered by the latter minerals. These findings imply that the groundwater was in a state of redox disequilibrium. They also indicate that, under more oxidizing conditions, the aqueous concentrations of many of the trace elements would not be determined by equilibrium with host minerals containing those elements as essential components, but rather by their distributions between the aqueous phase and adsorption sites on iron and/or manganese oxides, hydrated Al and Mg silicates or organic matter, or on the exchange sites on cationic or anionic clays.

4.3. Evolution of calcite saturation indices during CO_2 injection

Examination of core material from the ZERT site shows that coatings of secondary calcite are ubiquitous in the section below the water table from which groundwater samples were drawn for analysis. It would therefore not be surprising if a thermodynamic analysis showed that initial groundwater samples taken prior to injection of CO_2 were saturated with respect to calcite. However, the shallow subsurface environment at the ZERT site is subject to perturbations due to seasonal and long-term fluctuations in water table elevation due to infiltration of rainwater, evapotranspiration from the vadose zone, capillary transport, bio-metabolism and temperature. That some or all of these processes are operative is evident from the detection of a caliche horizon within the vadose zone approximately one meter below the surface.

Figure 5 shows the calculated saturation indices of calcite and calculated $P(CO_2)$ for the period under investigation. The increase in ambient $P(CO_2)$ leads to undersaturation of the

groundwater with respect to calcite. The fact that the undersaturation increases and persists for a while after CO_2 injection indicates that the rate of calcite dissolution is insufficient to maintain equilibrium. The trend is irregular and shows considerable scatter, which would be expected of a system where samples are taken from different wells in a soil system that is laterally heterogeneous. Also plotted on Figure 5 are three trend lines. Trend line A displays the approximate path taken with respect to calcite resaturation as $P(CO_2)$ increases. This path would vary depending on the rate of CO_2 saturation of the groundwater, the kinetics of calcite dissolution, calcite surface area and abundance, and groundwater flow rates. Path A is constrained by the other two trend lines. Trend line B is the path taken under static conditions where resaturation of calcite occurs after instantaneous saturation of the groundwater with CO_2 at a pressure of 1 bar, the approximate limit of saturation expected at the ZERT site. Trend line C assumes that no dissolution of calcite takes place upon uptake of CO_2. It is evident that about half of the water samples taken between July 7 and July 17, 2008 reflect this latter condition (close to trend line C), and that significant dissolution of calcite only started to occur after log $P(CO_2)$ exceeded ≈ -0.7, equivalent to 0.2 bar.

4.4. Principal Component Analysis

An initial step in identifying those groups of chemical constituents that respond similarly to CO_2 intrusion at the site is to perform a principal component analysis (PCA). PCA is a statistical tool for the interpretation of datasets consisting of multiple observations in many samples. The aim is to reduce the observed relations among the variables to simpler linear relations between fewer variables, called principal components, which are not correlated, but which explain the total variance of the data. In the context of the present study, PCA does not identify what each principal component relates to in terms of the chemical processes taking place in the field.

However, it does identify which chemical species are strongly correlated with a given principal component, and this in itself provides a basis for hypothesizing the relationship of each principal component to a chemical process. Unequivocal assignment of a specified chemical process to the derived principal components is plausible only in conjunction with an independent evaluation of the mineralogy, interpretation of measured soil chemical and physical properties, and independent thermodynamic and kinetic analyses. As ultimately demonstrated in this study, the interpretation can be further strengthened through an independent comparison of modeled predictions of groundwater composition with field observations (Section 5).

Information on ten principal components is presented in Table 3. The first four principal components (PC1 – PC4) explain over 80% of the variance, whereas principal components No. 5 (PC5) and No. 6 (PC6) explain another 10%. With respect to PC1, nine of the chemical species show correlations of 0.9 and above, and another six show correlations between 0.8 and 0.9. With the exception of HCO_3, Li and Na, all of the remainder are probably present as divalent cations, or divalent hydroxy-cations of trivalent species, such as alkali earth metals (Mg, Ca, Sr, Ba), B, Al, and Cr. PC2 correlates strongly only with F, and relatively weakly with As, Se and Mo, all potential oxy-anionic species, and inversely, but weakly with H and K. PC3 correlates inversely with Mn, Co and Cl, and directly with As, NO_3 and PO_4. PC4 correlates with Cl and SO_4. Correlations of chemical species with the remaining six components are for the most part weak and are of questionable significance.

The primary principal components (PC1-PC4) probably relate to a chemical process that takes place rapidly, given the short interval over which the analyses were taken, and considering the fact that a close logarithmic relationship is observed with respect to HCO_3^- in PC1 (for example, the correlation between Sr and HCO_3^- as shown in Figure 4). The most likely short-

term processes are, in order of reaction rate: cation exchange, adsorption/desorption, dissolution of carbonates and metastable Fe hydroxides and fougerite, some homogeneous redox reactions in the aqueous phase, and pore water infiltration from the vadose zone.

5. Geochemical model

Geochemical simulations were conducted to further evaluate the water chemistry trends observed during the test and identify likely mobilization processes. Our starting point for the modeling study is the hypothesis drawn from the PCA study discussed earlier, which suggests that cation exchange and sorption processes, together with dissolution of carbonates, may be the main factors driving the geochemical response to CO_2 injection. The simulations were conducted without considering transport (i.e., in "batch" mode). As mentioned earlier, additional modeling work incorporating transport processes was not warranted because of the relatively limited set of field data, as well as uncertainties regarding groundwater flow and CO_2 transport, subsurface heterogeneity, and rainfall effects. It should be noted that the measured geochemical changes were fairly rapid and similar in magnitude in most observation wells. Furthermore, our PCA analyses revealed similar groundwater chemistry responses to CO_2 injection at the different monitored locations. This suggests that "batch" simulations, focused solely on reactive processes induced by increasing levels of CO_2, are a good modeling approach in this case, with little more to gain from more sophisticated attempts to simulate details of multi-phase reactive transport. The simulations were performed using TOUGHREACT V2 (Xu et al., 2010), which was enhanced through incorporation of surface complexation to compute the distribution of adsorbed chemical species on mineral surfaces (e.g., Zheng et al., 2009; Apps et al., 2010).

5.1. Model setup

In the "batch" geochemical model, CO_2 was (numerically) injected into the modeled system, and simulation results were examined as a function of pH. CO_2 was injected into the model grid block until the computed pH value fell from an initial value ~7.1 to a value near 5.8, consistent with the field measurements. Instantaneous equilibration of gaseous CO_2 with the aqueous phase was assumed. Simulations were carried out assuming an initial temperature of 10°C and an initial pressure close to atmospheric values. Other elements of the model are described below.

5.2. Initial conditions

The initial water chemical composition for the model (Table 1) was taken from the average of five water samples, with initial pH adjusted from 6.7 to 7.1 so that our calculation covers the pH range of all samples considered in this study. An initial aqueous speciation calculation was conducted with the geochemical modeling package EQ3 (Wolery, 1993) to verify charge balance and evaluate the water saturation with respect to several minerals. The initial partial pressure of CO_2 in the groundwater was calculated to be 2.5×10^{-2} bar. Furthermore, calcite was close to saturation, i.e., SI(calcite) ≈ –0.1 (–0.3 at pH 6.7). The minerals considered in the geochemical model, as well as the volume fractions assigned to each mineral, were estimated on the basis of the mineralogical descriptions and are listed in Appendix A. With the exception of calcite and fougerite , the reaction rates of most of these minerals are so slow that they can be considered essentially non-reactive during the short test period; thus, their presence and chemical parameter choices do not affect model results.

As pointed out earlier, redox is not likely to have reached equilibrium in this shallow, low-temperature aquifer system. This complicates the use of geochemical models such as the one applied here, because these models rely on the assumption of redox equilibrium to calculate

the distribution of redox-sensitive species. Using the average water composition in Table 1, a pe of 9 is computed assuming the initial redox state of the groundwater is controlled by the coexistence of fougerite and ferrihydrite (as $Fe(OH)_3$). This contrasts with measured Eh values (Kharaka et al., 2010) corresponding to pe ~ 2.5-3.4. However, these measurements likely reflect mixed potentials that are not representative of a specific redox couple, and that may be biased by the redox sensor. Because the choice of pe affects model results for redox-sensitive species (i.e., most metals), the model was run assuming two alternative pe values (2 and 9) covering the range expected to be most relevant to site conditions. Given these uncertainties, and the fact that redox equilibrium is assumed in the simulations, model results regarding redox species should be viewed as qualitative rather than quantitative.

5.3. Chemical reactions

Chemical reactions considered in the model include aqueous complexation, cation exchange, adsorption/desorption, and mineral dissolution/precipitation. The thermodynamic data for these reactions and their sources are given in Appendix B. A Gouy-Chapman double diffuse layer surface complexation model is used to calculate adsorption/desorption (e.g., Langmuir, 1997). Hydrous ferric iron oxide (HFO) is assumed to be the sorbent in our simulations, and is modeled as ferrihydrite with the approximate formula $Fe(OH)_3$. Sorption constants and sorbent properties are taken from Dzombak and Morel (1990), with the strong site density equal to 8.5×10^{-8} mol sites/m^2, the weak site density equal to 3.4×10^{-6} mol sites/m^2, and the pure sorbent surface area equal to 600 m^2/g. Adsorption/desorption reactions are largely controlled by the total amount of sorption sites (expressed through the "site concentration"), which is the product of site density, sorbent specific surface area, and the total amount of sorbent. The model sensitivity to the total amount of sorption sites can be evaluated by varying any one of these three parameters in the

product. As discussed later, this is done, here, by varying surface area (using values of 0.06, 6, and 600 m^2/g) with a fixed (assumed) sorbent concentration (1% by volume of total solids, as $Fe(OH)_3$).

The cation exchange capacity (CEC) is another key parameter affecting exchange reactions. No measured CEC data were available for the sediments at the ZERT site prior to the start of this study. Therefore, model simulations were run using a range of CEC values (1.2, 6, and 12 meq/100g) covering a span typical of values for gravelly sediments (e.g., Steefel et al., 2003; Malcolm and Kennedy, 1970). CEC measurements conducted after the start of this study indicate values of ~ 9 meq/100g in the zone of interest at the ZERT site, consistent with the range of values selected in the model.

Minerals are set to react under kinetic constraints, with rate laws and parameters described in Appendix A. However, as noted above, the model is only sensitive to the dissolution rates of calcite and fougerite; other minerals are essentially non-reactive because of the short time frame of the test and the slow reaction rates (Appendix A). The dissolution rate of calcite is critical because the increase of Ca^{+2} resulting from calcite dissolution affects cation exchange, which may be responsible for the increase in the concentration of some elements upon CO_2 release, as discussed later. According to Kaufmann and Dreybrodt (2007), the dissolution of calcite can be described using a fast or a slow rate constant depending on the ratio of calcium concentration in the solution to the calcium concentration in equilibrium with calcite (C/C_{eq}) at a given CO_2 partial pressure. Kaufmann and Dreybrodt (2007) reported that when the ratio (C/C_{eq}) is <0.3, a fast rate constant applies, whereas when $C/C_{eq} > 0.3$, a slow rate constant applies. In the current model, C/C_{eq} is about 0.4–0.5, and thus the slow rate constant given by Kaufmann and Dreybrodt (2007) is adopted (1.6×10^{-6} $mol/m^2/s$). Svensson and Dreybrodt (1992)

investigated the dissolution kinetics of calcite in CO_2-water systems approaching calcite equilibrium and gave a rate constant k of $1.6\times10^{-6} – 2.2\times10^{-6}$ mol/m^2/s at C/C_{eq} values around 0.6–0.8. Gledhill and Morse (2006) reported that the dissolution rate depends on brine composition, $P(CO_2)$ (0.1–1 bar), and temperature, and provided a multiple regression model for the rate constant (k). Applying their regression model to our simulation conditions, a rate constant from 4.4×10^{-6} to 2.2×10^{-5} mol/m^2/s is calculated. Jordan and Rammensee (1998) gave a dissolution rate of 1.5×10^{-6} mol/m^2/s on the calcite surface obtained by scanning force microscopy, which corresponds well to the rates obtained from batch experiments. Therefore, these various published dissolution rates for calcite at lower levels of undersaturation are all quite consistent with the value selected for this study. Surface area comes into play in the rate law (equation A-1) and thus directly affects reaction rates. The calcite surface area in this study (0.365m^2/g) was taken from Anderson (1968).

The dissolution of fougerite only affects the simulation at pe values < 9, because this mineral is assumed at equilibrium with the solution at pe=9, as discussed earlier. The dissolution of other Fe minerals was not considered for simplicity. The rate constant for fougerite and its surface area ($1.9\ 10^{-9}$ mol m^{-2} s^{-1}, 22.3 m^2/g) were calibrated to approximately reproduce the observed Fe concentrations. The calibration was conducted for a pe=2, the lowest pe value considered in this study.

5.4 Modeled Scenarios

Because of the uncertainty regarding critical geochemical parameters, three alternative models (A, B, and C) are considered to evaluate whether cation exchange and/or adsorption/desorption reactions can explain observed trends in groundwater quality during the test:

- Model A considers the full set of exchange and adsorption/desorption reactions involving both cations and anions (Tables A2 and A3). In this model, an initial pe of 9 is assumed. The surface area of the sorbent and CEC of the exchanger are taken as the mid-values in the range considered, i.e., 6 m^2/g and 6 meq/100g, respectively.
- Model B is the same as Model A except that adsorption/desorption of cations is not considered. Sorption reactions for anions are still considered, and the initial pe value of 9 is unchanged from Model A. By comparing Model A and Model B, the effect of cation sorption reactions (versus exchange plus sorption) can be evaluated.
- Model C is equal to Model B, but uses an initial pe of 2. The sensitivity of model results to the initial redox potential can be evaluated by comparing the results of Model C with those of Model B.

The groundwater analyses and the PCA study discussed earlier suggest a correlated fast response of metal cations to the CO_2 release, together with a different correlated response for metal anions. On the basis of these observations, it is postulated that the trace metal cation response is related to exchange processes, but that the response of anionic species is related to adsorption/desorption processes. Therefore, Model B is considered as the base-case model since it considers sorption reactions only for anionic species.

5.5. Results and discussion

5.4.1. pH

Previous modeling studies of CO_2 leakage into potable groundwater aquifers (e.g., Wang and Jaffe, 2004; Apps et al., 2010; Wilkin et al., 2010) have indicated that the dissolution of carbonate minerals (mainly calcite) can strongly buffer the pH decrease accompanying elevated CO_2 concentration in water (from the dissociation of carbonic acid). Protonation/deprotonation

on mineral surfaces (e.g., clay minerals) can also buffer pH (e.g., Sposito, 1989). In the present model, the dissolution of calcite and H^+ buffering through protonation via cation exchange and surface complexation all contribute to buffering pH, but to a different degree. Figure 6 shows the pH calculated by different combinations of these chemical processes, using Model B. A simulation without carbonate minerals leads to a lower pH than the case where the presence of carbonates is assumed, but the former is only marginally higher than the simulation without any buffering. This suggests that at the ZERT site, dissolution of calcite is the principal pH buffering process, whereas the H^+ exchange by clays does not affect pH significantly, mainly because exchangeable H^+ occupies too little sites to make any difference on pH and the pH decrease is moderate.

5.4.2. Major cations and alkaline earth metals

The groundwater at the ZERT site responds promptly to the release of CO_2. The pH falls from near 7 to less than 6 within 1 or 2 days from the start of injection, and a significant increase in major cations is observed before the first rainfall occurs, about 10 days later. In such a short period, only the kinetic rates for rapidly dissolving minerals such as calcite and fougerite are important. As noted earlier, the dissolution rate of calcite is critical, because the resulting increase of Ca^{+2} induces cation exchange, which may be responsible for the increases in major cations and most trace metals. The kinetic rate for calcite adopted in this study falls within the lower range of published values and yields results consistent with measured changes in calcium concentration observed in the field, as shown in Figure 7 for Model A. If a higher calcite dissolution rate is used, such as the value of 2.2×10^{-5} mol/m^2/s given by Gledhill and Morse (2006), the computed calcium concentration is overestimated compared to the measured data (Figure 7).

As pH decreases, calcite dissolves and releases Ca^{+2} into the aqueous phase. Aqueous Ca^{+2} in turn exchanges with the exchangeable cations on the exchanger. As a result, the concentrations of all the major cations increase in solution. Figure 8 shows the evolution of K as an example. Another possible contribution to the observed increase in the concentrations of major cations could be the release of cations from sorption sites. However, simulations show that Model B (which does not consider sorption reactions for cations) leads to almost the same results as Model A (which considers the adsorption/desorption of cations in addition to exchange reactions). This suggests that cation exchange alone could control the evolution of major cations in response to the CO_2 injection at the ZERT site. Figure 9 shows a reasonable match between the measured and computed Sr^{+2}, which indicates that this alkaline earth metal may also be mainly controlled by the Ca^{+2}-driven exchange reactions. It cannot be ruled out, however, that the release of Sr^{+2} may also be the result of calcite dissolution, as this element is a common trace constituent in calcite.

5.4.3. Trace metal cations

Figures 10 through 13 show the calculated and observed concentrations for Pb, Cd, Cu, and Zn using Model A and Model B. Results for Model C do not significantly differ from results of Model B, except for Fe. Model B yields reasonable agreement with measured data, suggesting that the Ca^{+2}-driven cation exchange alone can explain the observed trace metal response to CO_2 injection. Additional model predictions suppressing cation exchange, while considering sorption reactions for both cations and anions overestimate the predicted concentrations of all metals except Cd. Model A, which considers both adsorption/desorption and cation exchange reveals the interplay of the two chemical processes: When desorption dominates over exchange (e.g., as for Zn), cation exchange counter-balances and limits the effect of desorption; conversely, when

exchange dominates over desorption (e.g., as for Cd), the effect of cation exchange is limited by sorption. Overall, the consideration of adsorption/desorption reactions for trace-metal cations in the model does not improve the model predictions relative to the measured data. It should be noted that the model results would be better constrained if critical geochemical parameters, such as the CEC, sorbent concentration, and specific surface area, were available from site-specific investigations and therefore some caution is required when interpreting the model results.

Figure 14 shows the predicted Fe concentrations for the different simulated scenarios. Model C, with an initial pe of 2, shows the best fit because the rate of fougerite dissolution was calibrated to the observed trend of Fe concentrations assuming a pe value of 2. The predicted dissolution of fougerite is minimal with Models A and B because at the pe value considered in these models (pe=9) this mineral is essentially equilibrated with the aqueous solution. When fougerite is not allowed to dissolve in Model C, the predicted Fe concentrations remain low. This observation, together with the comparison of Model C with Models A and B, suggests that adsorption/desorption or exchange reactions do not play a significant role in the evolution of iron, and that dissolution of a Fe-bearing mineral is likely to have generated the observed increases in Fe concentrations. This is consistent with the finding from the PCA (Section 4.2) that the behavior of iron does not correlate with the component associated with ion exchange.

5.4.5. Anions

Another effect of CO_2 dissolution in groundwater is the increase of aqueous bicarbonate (HCO_3^-) concentrations (Figure 15). This increase modifies the distribution of adsorbed anionic species on HFO (e.g., Appelo et al., 2002). Table 4 lists the total adsorbed concentrations associated with the anions and H^+ considered in the surface complexation reactions on HFO in Model B, and their computed maximum change upon CO_2 injection. For each listed component in Table 4, the

total adsorbed concentration represents the summation of the concentrations of all surface species for that component (Table A3). Initially, adsorbed carbonate occupies a large proportion of the sorption sites (about 50%). The increase in HCO_3^- and pH decrease resulting from the dissolution of CO_2 lead to increased adsorption of carbonate on the HFO surface. As a result, some anionic species are displaced into the aqueous phase.

Figure 16 shows the aqueous concentration of As computed with Models A, B and C. Even though the scatter in the arsenic measurements is large, the similarities between computed and observed As concentrations suggest that carbonate-initiated desorption could be a controlling process for this element, as has been observed in other systems (Appelo et al., 2002; Frau et al., 2008). The difference in simulation results between Models A and B is also caused by the competition for sorption sites. The adsorption/desorption of arsenic is controlled by two types of surface species, HFO_wH_2AsO_4 which leads to adsorption as pH drops, and HFO_w$HAsO_4^-$ which results in desorption when carbonate is adsorbed. The increase or decrease of aqueous arsenic concentration is the net effect of the variation of these two surface species. In Model B, as the cations are not included in the adsorption/desorption reaction, more sites are initially available for carbonate sorption, allowing for a relatively stronger desorption of As, which leads to overall higher aqueous As concentration. In Model A, on the other hand, less sites are initially available for carbonate sorption. Therefore relatively less desorption of arsenic occurs, which eventually results in overall lower aqueous As concentration. In Model C, although the initial pe is lowered from 9 to 2, As(V) is still the dominant species and thus there is no significant difference in As concentration between this model and Model B.

Figure 17 shows the measured and computed aqueous concentrations of selenium for Models B and C. The results of Model A are not shown because they are very similar to those in

Model B. Model B clearly overestimates the predicted concentrations. Model C, while overestimating concentrations, provides a better fit to the measured data. The reason is that in Model B, the dominant selenium species is Se(VI), whereas Se(IV) dominates in Model C.

The concentration of aqueous phosphate (Figure 18) decreases with the decrease in pH because anionic adsorption occurs (Table 4). The concentrations of adsorbed HFO_sPO_4^{-2} and HFO_wPO_4^{-2} are computed to decrease as carbonate species adsorb. However, the concentrations of HFO_sH_2PO_4 and HFO_wH_2PO_4 increase as the pH falls. This increase is greater than the decrease in HFO_s PO_4^{-2} and HFO_w PO_4^{-2} concentrations, and as a result the concentration of phosphate in the groundwater actually falls. The evolution of phosphate is not sensitive to the changes of redox condition, and thus differences in Models B and C are insignificant.

5.4.6 Model B sensitivity to CEC and sorption site concentration

A sensitivity study was conducted with Model B without adsorption/desorption reactions to isolate the effect of cation exchange. Three CEC values (1.2, 6 and 12 meq/100 g) were considered, covering a typical range for gravelly sediments (e.g., Steefel et al., 2003; Malcolm and Kennedy, 1970), and focusing on sodium and potassium as the major exchangeable cations (magnesium is not examined because it is mainly controlled by the dissolution of dolomite, which is assumed to be essentially non-reactive here). The sensitivity of predicted Na concentrations to input CEC values is shown in Figure 19. These simulations show that the three considered CEC values yield results that fall within the scatter of the data.

As mentioned earlier, the amount of sorption sites available for adsorption/desorption reactions (expressed though the site concentration) is defined by the product of sorption site

density, sorbent specific surface area, and sorbent amount (ferrihydrite in this case). Varying any of these three parameters yields proportional variations in site concentrations. Here, we chose surface area as the variable parameter, keeping the other two parameters at fixed values. The specific surface area of 600 m^2/g adopted in Dzombak and Morel (1990) is quite high, and represents an upper bound considering that surface area measurements are often determined in experiments that use iron hydroxide suspension gel. In natural conditions, iron hydroxides occur in assemblages with other minerals and can be coated by less reactive minerals, which could significantly reduce the surface area available for reaction, by orders of magnitude. For these reasons, three specific surface area values (600, 6 and 0.06 m^2/g) are considered in the sensitivity analysis. This is accomplished using Model A, but without cation exchange reaction to isolate sorption effects.

In general, a surface area of 6 m^2/g yields model results that are most consistent with the measured data, as shown in Figure 20 for Cd and Figure 21 for HPO_4^{-2}. However, according to Figure 22, even a surface area as small as 0.06 m^2/g gives rise to a significant overestimation of predicted Pb concentration. This is because Pb forms very strong surface complexes, and equilibration of initial (measured) Pb concentrations with sorption sites yields a high Pb loading in the sediments. The high initial sorbed Pb concentration then results in elevated lead concentrations in the groundwater upon the pH decrease induced by CO_2 injection. As seen earlier with Model B (Figure 10), the observed trend in lead concentrations is much better captured using cation exchange than sorption.

6. Summary and Conclusions

Rapid and systematic increases in the aqueous concentrations of major and trace elements were observed in response to shallow CO_2 injection at the MSU-ZERT field test (Kharaka et al., 2010). These water quality changes were interpreted using principal component analyses and multicomponent reaction path ("batch") geochemical simulations considering aqueous speciation, ion exchange, surface complexation, and mineral precipitation/dissolution. The relative contributions of these processes to metal mobilization upon CO_2 injection were investigated. Measured concentrations of aqueous species in groundwater before and during CO_2 injection, prior to rainfall, were compared to model results. Reasonable matches between measured data and model results suggest that (1) calcite dissolution could be the primary process buffering pH and releasing Ca^{+2} in groundwater, (2) the increase in the concentrations of major cations and trace metals except Fe could be explained by Ca^{+2}-driven exchange reactions, (3) the release of anions from adsorption sites due to competing adsorption of bicarbonate could explain the concentration trends of most anions, and (4) the dissolution of reactive Fe minerals (such as fougerite) could explain the increase in total Fe concentration.

Because of the lack of site-specific data for key model parameters such as exact sorbent type and concentration, sorption constants, mineral surface areas, and redox state, the simulations relied heavily on assumed and/or typical but not site-specific values for these critical parameters. As a result, for a chemical system as complex as that at the ZERT site, multiple combinations of modeled processes and reasonable input parameters ranges could explain the field observations. The non-uniqueness of our geochemical model clearly points to the need for a comprehensive characterization of the sediment-metal associations in the subsurface and the redox conditions to better constrain model results. Consequently, our modeling effort should be regarded as an

exercise that yields a plausible, but uncertain interpretation of the chemical processes taking place in response to increasing ambient CO_2 concentrations in shallow groundwater systems.

It should be noted that potable aquifers are usually deeper and less likely to be impacted by transient interactions with overlying soil zones or atmospheric precipitation events than the ZERT site. It is anticipated that higher hydraulic pressures in deeper aquifer would result in a higher pCO2 and increased CO_2 dissolution in groundwater, relative to observations at the ZERT site, and thus could result in a more pronounced pH decrease and possibly a more significant release of contaminants (e.g. Kharaka et al., 2009; Caroll et al., 2009). Furthermore, the controlled-release period of about four weeks may have been too short to test the importance of slower release mechanisms for trace metals, such as by dissolution of trace-metal-bearing primary minerals. Targeted controlled-release experiments should be carried out to further our understanding of possible groundwater contamination from CO_2 intrusion, ideally in deeper aquifers more representative of the majority of our groundwater resources, and with longer injection period to monitor contaminant release from short-term and long-term geochemical processes. Additional studies of natural analogues with a focus on trace metal mobilization would also be useful to further assess the risk of groundwater contamination from CO_2 leakage.

Acknowledgment

This research was conducted within the MSU-ZERT project directed by Lee Spangler and managed by Laura Dobeck, MSU, Bozeman, MT. We thank the entire MSU-ZERT team and participating organizations for creating a supportive and exciting research environment. We also thank Toby Day of the Montana State University Extension Service for drawing our attention to precipitation records at the Bozeman airport. This research was funded primarily by the Electric

Power Research Institute, EPRI. LBNL authors were partially supported by the U.S. DOE and LBNL under Contract No. DE-AC02-05CH11231.

References

Aiuppa, A., Federico, C., Allard, P., Gurrieri, S. and Valenza, M., 2005. Trace metal modeling of groundwater-gas-rock inter-actions in a volcanic aquifer: Mount Vesuvius, Southern Italy. Chemical Geology 216, 289-311.

Ambats, G., Apps, J. A., Beers, S., Birkholzer, J. T., Gullickson, K. S., Herkelrath, W. N., Kakouros, E., Kharaka, Y. K., Spangler, L. H., Spycher, N., Thordsen, J. and Zheng, L., 2009. Groundwater chemistry changes as a result of CO_2 injection at the ZERT field site in Bozeman, Montana. Lawrence Berkeley National Laboratory. Project Report LBNL-2931E.

Anderson, T. F. 1968. Surface area measurement in calcite grains by isotopic exchange with C^{14}-labeled carbon dioxide. Geochimica et Cosmochimica Acta, 32,1177-1186.

Appelo, C. A. J., Van Der Weiden, M. J. J., Tournassat, C. and Charlet, L., 2002. Surface complexation of ferrous iron and carbonate on ferrihydrite and the mobilization of arsenic. Environmental Science & Technology 36(14), 3096-3103.

Appelo, C. J. A. and Postma, D., 1994. Geochemistry, groundwater and pollution. Rotterdam, Netherlands, A.A.Balkema.

Apps, J. A., Zheng, L., Zhang, Y., Xu, T. and Birkholzer, J. T., 2010. Evaluation of groundwater quality changes in response to CO_2 leakage from deep geological storage. Transport in Porous Media 82(1), 215-246.

Arnórsson, S., Hurtig, N., Gysi, A. P., Bird, D. K. and O'Day, P. A., 2010. Carbon dioxide waters in Iceland: A natural analogue to CO_2 sequestration in basaltic aquifers. Water-Rock Interaction. Birkle and Torres-Alvarado. Guanajuato, Mexico, 2010 Taylor & Francis Group, London, ISBN 978-0-415-60426-0.

Bachu, S., 2000. Sequestration of CO_2 in geological media: criteria and approach for site selection in response to climate change. Energy Conv. Manag. 42, 953–970.

Birkholzer, J. T., Apps, J. A., Zheng, L., Zhang, Y., Xu, T. and Tsang., C.-F., 2008. Research Project on CO_2 Geological Storage and Groundwater Resources: Water Quality Effects Caused by CO_2 Intrusion into Shallow Groundwater. Berkeley, CA, Lawrence Berkeley National Laboratory. Technical Report LBNL-1251E.

Bradbury, M. H. and Baeyens, B., 2005. Modelling the sorption of Mn(II), Co(II), Ni(II), Zn(II), Cd(II), Eu(III), Am(III), Sn(IV), Th(IV), Np(V) and U(VI) on montmorillonite: Linear free energy relationships and estimates of surface binding constants for some selected heavy metals and actinides. Geochimica et Cosmochimica Acta 69(4), 875-892.

Carroll, S. 2009. Trace metal release from Frio Sandstone reacted with CO_2 and 1.5N NaCl brine at 60 ^{o}C. Eighth Annual Carbon Capture & Sequestration Conference, Pittsburgh, PA.

Carroll, S., Hao, Y. and Aines, R., 2009. Geochemical detection of carbon dioxide in dilute aquifers. Geochemical Transactions 10(4), 1-18.

Charlet, L. and Tournassat, C., 2005. Fe(II)–Na(I)–Ca(II) Cation exchange on montmorillonite in chloride medium: evidence for preferential clay adsorption of chloride – metal ion pairs in seawater. Aquatic Geochemistry 11, 115-137.

Dzombak, D. A. and Morel, F. M. M., 1990. Surface complexation modeling-hydrous ferric oxide. New York, John Wiley & Sons.

Drummond, S. E. and Ohmoto, H., 1985. Chemical evolution and mineral deposition in boiling hydrothermal systems. Economic geology 80(1), 126-147.

Flaathen, T. K., Gislason, S. R., Oelkers, E. H. and Sveinbjörnsdóttir, Á. E., 2009. Chemical evolution of the Mt. Hekla, Iceland, groundwaters: A natural analogue for CO_2 sequestration in basaltic rocks. Applied Geochemistry 24(3), 463-474.

Frau, F., Biddau, R. and Fanfani, L., 2008. Effect of major anions on arsenate desorption from ferrihydrite-bearing natural samples. Applied Geochemistry 23(6), 1451-1466.

Gledhill, D. K. and Morse, J. W., 2006. Calcite dissolution kinetics in Na–Ca–Mg–Cl brines. Geochimica et Cosmochimica Acta 70, 5802-5813.

Jordan, G. and Rammensee, W., 1998. Dissolution rates of calcite (10#14) obtained by scanning force microscopy: Microtopography-based dissolution kinetics on surfaces with anisotropic step velocities. Geochimica et Cosmochimica Acta, 62, 941-947.

Kaufmann, G. and Dreybrodt, W., 2007. Calcite dissolution kinetics in the system $CaCO_3$–H_2O–CO_2 at high undersaturation. Geochimica et Cosmochimica Acta 71, 1398-1410.

Keating, E. H., Fessenden, J., Kanjorski, N., Koning, D. J. and Pawar, R., 2010. The impact of CO_2 on shallow groundwater chemistry: observations at a natural analog site and implications for carbon sequestration. Environmental Earth Sciences 60(3), 521-536.

Kharaka, Y. K., Cole, D. R., Hovorka, S. D., Gunter, W. D., Knauss, K. G. and Freifeld, B. M., 2006. Gas-water-rock interaction in Frio formation following CO_2 injection: implications for the storage of greenhouse gases in sedimentary basins. Geology 34, 577-580.

Kharaka, Y. K., Thordsen, J. J., Hovorka, S. D., Nance, S., Cole, D. R., Phelps, T. J. and Knauss, K. G., 2009. Potential environmental issues of CO_2 storage in deep saline aquifers: Geochemical results from the Frio-I brine pilot test, Texas, USA. Applied Geochemistry 24, 1106-1112.

Kharaka, Y. K., Thordsen, J. J., Kakouros, E., Ambats, G., Herkelrath, W. N., Beers, S. R., Birkholzer, J. T., Apps, J. A., Spycher, N. F., Zheng, L., Trautz, R. C., Rauch, H. W. and Gullickson, K. S., 2010. Changes in the chemistry of shallow groundwater related to the 2008 injection of CO_2 at the ZERT field site, Bozeman, Montana. Environmental Earth Sciences 60(2), 273-284.

Knauss, K.G., Johnson, J.W., Steefel, C.I., 2005. Evaluation of the impact of CO_2, co-contaminant gas, aqueous fluid, and reservoir rock interactions on the geologic sequestration of CO_2. Chemicalo Geology 217, 339-350.

Langmuir, D., 1997. Aqueous environmental geochemistry, Prentice Hall.

Lasaga, A. C., Soler, J. M., Ganor, J., Burch, T. E. and Nagy, K. L., 1994. Chemical weathering rate laws and global geochemical cycles. Geochimica et Cosmochimica Acta 58, 2361-2368.

Lewicki, J., Oldenburg, C., Dobeck, L. and Spangler, L. H., 2007. Surface CO_2 leakage during the first shallow subsurface CO_2 release experiment. Geophys Res Lett 34, L24402.

Lindsay W.L. and Walthall P.M., 1996. The solubility of aluminum in soils. Chapter 8 in (Sposito G., ed.) The Environmental Chemistry of Aluminum. Lewis Publishers, CRC Press, Boca Raton, Florida, 467 p.

Little, M. G. and Jackson, R. B., 2010. Potential impacts of leakage from deep co_2 geosequestration on overlying freshwater aquifers. Environmental Science & Technology 44(23), 9225-9232.

Lu, J. M., Partin, J. W., Hovorka, S. D. and Wong, C., 2010. Potential risks to freshwater resources as a result of leakage from CO_2 geological storage: a batch-reaction experiment. Environmental Earth Sciences 60(2), 335-348.

McGrath, A. E., Upson, G. L. and Caldwell, M. D.-. 2007. Evaluation and mitigation of landfill gas impacts on cadmium leaching from native soils. Ground Water Monitoring & Remediation 27(99-109).

Muller, B. and Sigg, L., 1991. Adsorption of lead(ll) on the goethite surface: voltammetric evaluation of surface complexation parameters. Journal of Colloid and Interface Science 148(2), 517-532.

Oldenburg, C., Lewicki, J., Dobeck, L. and Spangler, L., 2010. Modeling gas transport in the shallow subsurface during the ZERT CO_2 release test. Transport in Porous Media 82(1), 77-92.

Palandri, J. and Kharaka, Y. K., 2004. A compilation of rate parameters of water-mineral interaction kinetics for application to geochemical modeling, US Geol. Surv. Open File report 2004-1068, 64p.

Smyth, R. C., Hovorka, S. D., Lu, J., Romanak, K. D., Partin, J. W., C., W. and Yang, C., 2009. Assessing risk to fresh water resources from long term CO_2 injection – laboratory and field studies. Energy Procedia 1(1957-1964).

Sonnenthal, E., Spycher, N., 2000. Drift-scale coupled processes model. Analysis and model report (AMR) N0120/U0110, Yucca Mountain Nuclear Waste Disposal Project, Lawrence Berkeley National Laboratory, Berkeley, California.

Sposito, G., Holtzclaw, K. M., Charlet, L., Jouany, C. and Page, A. L., 1983. Sodium-calcium and sodium-magnesium exchange on wyoming bentonite in perchlorate and chloride background ionic media. Soil Sci. Soc. Am. J. 47, 51-56.

Spangler, L. H., Dobeck, L. M., Repasky, K. S., Nehrir, A. R., Humphries, S. D., Barr, J. L., Keith, C. J., Shaw, J. A., Rouse, J. H., Cunningham, A. B., Benson, S. M., Oldenburg, C. M., Lewicki, J. L., Wells, A. W., Diehl, J. R., Strazisar, B. R., Fessenden, J. E., Rahn, T. A., Amonette, J. E., Barr, J. L., Pickles, W. L., Jacobson, J. D., Silver, E. A., Male, E. J., Rauch, H. W., Gullickson, K. S., Trautz, R., Kharaka, Y., Birkholzer, J. and Wielopolski, L., 2010. A shallow subsurface controlled release facility in Bozeman, Montana, USA, for testing near surface CO_2 detection techniques and transport models. Environmental Earth Sciences 60(2), 227-239.

Spycher, N. F. and Reed, M. H., 1989. Evolution of a broadlands-type epithermal ore fluid along alternative p-t paths - implications for the transport and deposition of base, precious, and volatile metals. Economic Geology 84(2), 328-359.

Steefel, C. I., Carroll, S., Zhao, P. and Roberts, S., 2003. Cesium migration in Hanford sediment: a multisite cation exchange model based on laboratory transport experiments. Journal of Contaminant Hydrology 67(1-4), 219-246.

Steefel, C. I. and Lasaga, A. C., 1994. A coupled model for transport of multiple chemical species and kinetic precipitation/dissolution reactions with applications to reactive flow in single phase hydrothermal system. . Am. J. Sci 294, 529–592.

Strazisar, B. R., Wells, A. W., Diehl, J. R., Hammack, R. W. and Veloski, G. A., 2009. Near-surface monitoring for the ZERT shallow CO_2 injection project. International Journal of Greenhouse Gas Control 3(6), 736-744.

Thordsen, J., 2011, Personal Communication.

Svensson, U. and Dreybrodt, W., 1992. Dissolution kinetics of natural calcite minerals in CO_2-water systems approaching calcite equilibrium. Chemical Geology 100, 129-145.

Tournassat, C., Ferrage, E., Poinsignon, C. and Charlet, L., 2004. The titration of clay minerals II. Structure-based model and implications for clay reactivity. Journal of Colloid and Interface Science 273, 234–246.

Wang, S. and Jaffe, P. R., 2004. Dissolution of a mineral phase in potable aquifers due to CO_2 releases from deep formations; effect of dissolution kinetics. Energy Conversion and Management 45, 2833-2848.

Wilkin, R. T. and Digiulio, D. C., 2010. Geochemical impacts to groundwater from geologic carbon sequestration: controls on ph and inorganic carbon concentrations from reaction path and kinetic modeling. Environmental Science & Technology 44(12), 4821-4827.

White, C. M., Smith, D. H., Jones, K. L., Goodman, A. L., LaCount, R. B., DuBose, S. B., zdemir, E., Morsi, B. I. and Schroeder, K. T., 2005. Sequestration of carbon dioxide in coal with enhanced coalbed methane recovery—A review. Energy Fuels 19, 659–724.

Wolery, T. J., 1993. EQ3/6, A software package for geochemical modelling of aqueous systems (Version 7.2). , Lawrence Livermore National Laboratory. UCRL-MA 110662.

Wolery, T. J. and Jove-Colon, C., 2007. Qualification of thermodynamic data for geochemical modeling of mineral-water interactions in dilute systems. Sandia National Laboratories. DOC.20070619.0007.

Xu, T, Apps, J.A., Pruess, K., 2004. Numerical simulation to study mineral trapping for CO_2 disposal in deep aquifers, Applied Geochemistry, 19, 917-936.

Xu, T, Apps, J.A., Pruess, K., 2005. Mineral sequestration of carbon dioxide in a sandstone-shale system. Chemical Geology, 217, 295-318.

Xu, T., Sonnenthal, E., Spycher, N. and Pruess, K., 2006. TOUGHREACT: A simulation program for non-isothermal multiphase reactive geochemical transport in variably saturated geologic media. Computers and Geosciences 32, 145-165.

Zerai , B., Saylor, B.Z., Matiso, G., 2006. Computer simulation of CO_2 trapped through mineral precipitation in the Rose Run Sandstone, Ohio. Applied Geochemistry, 21, 223-240.

Zheng, L., Apps, J. A., Zhang, Y., Xu, T. and Birkholzer, J. T., 2009. On mobilization of lead and arsenic in groundwater in response to CO_2 leakage from deep geological storage. Chemical geology 268(3-4), 281-297.

Zheng, Z. P., Zhang, G. X. and Wan, J. M., 2008. Reactive transport modeling of column experiments on the evolution of saline-alkaline waste solutions. J. Contam. Hydrol. 97(1-2), 42-54.

Table 1. Average initial water composition.

Species[a]	Concentration (molal)	Species	Concentration (molal)
pH	7.1	Ba^{+2}	8.01E-07
Ca^{+2}	2.20E-03	Cd^{+2}	1.43E-09
Mg^{+2}	1.03E-03	Co^{+2}	6.38E-09
Na^{+}	3.66E-04	Cu^{+2}	2.63E-08
K^{+}	1.43E-04	$H_2AsO_4^{-}$	6.93E-09
Fe^{+2}	2.70E-07	Mn^{+2}	1.19E-06
Al^{+3}	8.82E-08	Sr^{+2}	3.25E-06
SiO_2(aq)	4.80E-04	Zn^{+2}	4.95E-08
Cl^{-}	1.43E-04	$HSeO_3^{-}$	2.36E-08
HCO_3^{-}	6.70E-03	MO_4^{-2}	3.41E-09
SO_4^{-2}	7.57E-05	UO_2^{+2}	1.59E-08
NO_3^{-}	5.97E-06	$Cr(OH)_2^{+}$	4.32E-08
O_2(aq)	1.25E-27	HPO_4^{-2}	1.55E-06
Pb^{+2}	1.86E-10	Li^{+}	6.14E-07

[a]Species shown are primary species used in simulations. Other aqueous species are listed in Table B1. Except for pH, the concentration given include all aqueous species of one element (i.e., total concentrations).

Table 2. Saturation indices of common minerals with respect to groundwater at the ZERT site

Name	Formula	SI
Quartz	SiO2	+0.633
Opal-CT	SiO_2	-0.267
Gibbsite	$Al(OH)_3$	+0.402
Imogolite	$Al_2SiO_5.xH_2O$	-0.897
Kaolinite	$Al_2Si_2O_5(OH)_4$	+2.440
Beidellite-Ca	$Ca_{0.165}Al_{2.33}Si_{3.67}O_{10}(OH)_2$	+2.206
Smectite-Ca	$Ca_{0.145}Mg_{0.26}Al_{1.77}Si_{3.97}O_{10}(OH)_2$	+4.639
Montmorillonite-Ca	$Ca_{0.165}Mg_{0.33}Al_{1.67}Si_4O_{10}(OH)_2$	+2.175
Celadonite	$KMgAlSi_4O_{10}(OH)_2$	-0.355
Illite	$K_{0.6}Mg_{0.25}Al_{1.8}Al_{0.5}Si_{3.5}O_{10}(OH)_2$	+1.647
K-feldspar	$KAlSi_3O_8$	+1.009
Albite-low	$NaAlSi_3O_8$	-1.887
Calcite	$CaCO_3$	-0.283
Dolomite	$CaMg(CO_3)_2$	-3.196
Crandallite	$CaAl_3(PO_4)(OH)_5.H_2O$	-0.230
Barite	$BaSO_4$	-0.440
Ferrihydrite	$Fe(OH)_3$	~-4 to 0[a]
Fougerite(green rust)	$[2/9Fe^{II}(OH)_2.1/3Fe^{III}(OH)_2.4/9Mg(OH)_2]^{+1/3}[1/3A]^{-1/3}$ with $A = 2/3HCO_3^-.1/6CO_3^{-2}$	~-1 to 0[a]
Siderite	$FeCO_3$	~-2 to -4[a]

(a) Saturation indices computed for pe values of 2 to 9, respectively.

Table 3. Principal components derived from an analysis of groundwater chemical compositions for the period July 7 to July 17, 2008.

Component Loadings (correlations between initial variables and principal components)

Variable	PC 1	PC 2	PC 3	PC 4	PC 5	PC 6	PC 7	PC 8	PC 9	PC 10
H	0.774	-0.419	0.114	0.090	-0.289	-0.079	-0.111	0.051	0.279	0.018
Li	0.951	0.202	0.120	-0.010	-0.093	-0.063	0.071	-0.056	-0.026	0.086
Na	0.874	0.023	0.216	-0.246	0.223	-0.015	-0.064	0.062	0.113	-0.169
K	0.711	-0.500	0.071	0.245	-0.252	0.031	0.076	0.136	-0.005	-0.226
Mg	0.946	-0.215	0.111	-0.044	0.117	0.115	-0.059	0.029	-0.002	-0.002
Ca	0.914	-0.339	0.175	-0.014	0.018	0.062	0.023	0.051	-0.006	-0.070
Sr	0.931	-0.282	0.154	-0.060	0.084	0.077	-0.028	0.061	0.004	-0.044
Ba	0.902	-0.385	0.030	-0.053	0.025	0.127	-0.035	0.028	-0.032	-0.034
Mn	0.484	0.229	-0.735	-0.236	-0.001	-0.029	0.199	0.025	-0.033	-0.127
Fe	0.841	-0.169	-0.316	-0.257	0.156	0.019	0.088	-0.118	-0.164	0.044
Co	0.734	0.100	-0.537	-0.351	0.032	-0.015	0.077	-0.022	-0.070	0.045
Cu	0.857	0.201	0.275	0.113	0.176	-0.060	0.211	0.018	0.000	-0.116
Zn	0.282	0.372	0.221	-0.287	-0.268	0.663	0.076	0.317	-0.098	0.051
Cd	0.914	0.156	-0.013	0.080	-0.234	-0.173	0.163	0.030	0.044	0.119
Pb	0.872	0.287	0.007	0.155	-0.184	-0.233	0.109	0.089	-0.060	0.060
Al	0.972	-0.021	0.131	0.055	-0.054	-0.019	0.066	-0.004	-0.043	0.065
Cr	0.872	0.276	0.070	0.116	-0.298	-0.164	0.079	-0.061	-0.007	0.068
As	0.352	0.482	0.529	-0.105	0.044	0.174	-0.330	-0.410	-0.073	-0.109
Se	0.832	0.417	0.189	0.013	-0.142	0.001	-0.115	-0.228	-0.020	0.005
Mo	0.620	0.441	-0.058	0.196	0.313	-0.411	-0.150	0.166	-0.145	-0.143
U	0.497	-0.203	0.325	-0.258	0.562	-0.203	-0.126	0.194	0.086	0.208
F	-0.201	0.870	0.095	-0.056	0.047	0.006	-0.108	0.368	0.004	-0.045
Cl	0.385	0.035	-0.573	0.615	0.168	0.257	-0.102	0.029	-0.021	-0.081
Br	0.252	0.387	0.148	0.340	0.464	0.286	0.497	-0.140	0.275	0.046
NO3	-0.477	-0.303	0.547	0.195	0.083	-0.056	0.352	0.005	-0.431	0.026
PO4	-0.791	0.034	0.434	0.310	-0.094	-0.030	-0.125	0.165	0.027	0.012
SO4	0.631	-0.104	-0.347	0.406	0.217	0.245	-0.359	0.014	-0.153	0.179
HCO3	0.928	-0.271	0.141	-0.061	0.099	0.097	-0.032	0.065	-0.014	-0.007
SiO2	0.967	0.079	0.165	0.002	-0.079	0.028	-0.056	-0.076	-0.043	-0.009
B	0.910	0.172	-0.084	0.202	-0.223	-0.045	-0.061	0.031	0.038	0.107

LEGEND	
	> 0.9
	> 0.8
	> 0.7
	> 0.6
	> 0.5
	> 0.4

Table 4. Initial total concentrationsof each adsorbed components (C^i, before CO_2 injection) and their maximum change (Δ_{max}) computed at the lowest pH (Δ_{max} is negative for desorption and positive for sorption).

Adsorbed component	C^i (molal)	C^i (ppm)	Δ_{max} (molal)
H^+	2.2E-04	3.5E-02	-9.7E-05
sulfate	4.2E-04	6.6	-4.4E-05
Se	1.6E-07	2.0E-03	-1.6E-07
Mo	9.3E-07	1.4E-02	-3.2E-09
carbonate	7.5E-04	7.3	1.7E-04
As	2.9E-06	3.4E-02	-7.6E-09
P	7.4E-05	1.1E+00	1.1E-06

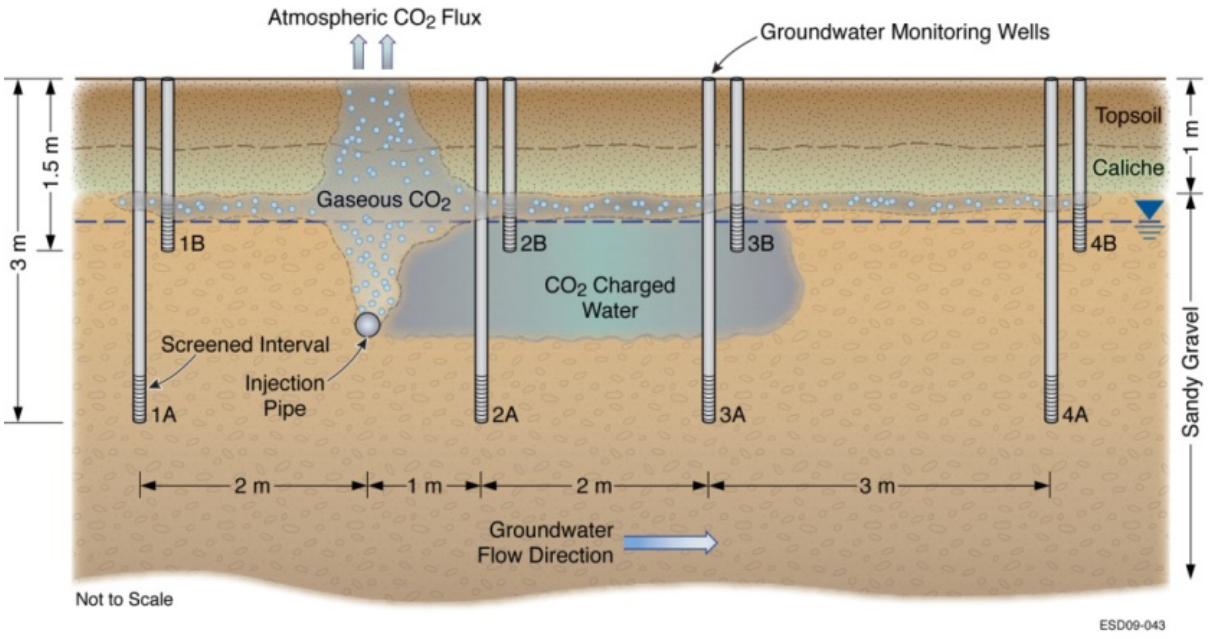

Figure 1. Schematic representation of CO_2 transport at the ZERT field site. The cross-section shown is along the axis of well pairs 1A/B, 2A/B, 3A/B, and 4A/B, roughly perpendicular to the injection pipe. Well pair 5A/B is a few meters off the cross-section, near well pair 2A/B.

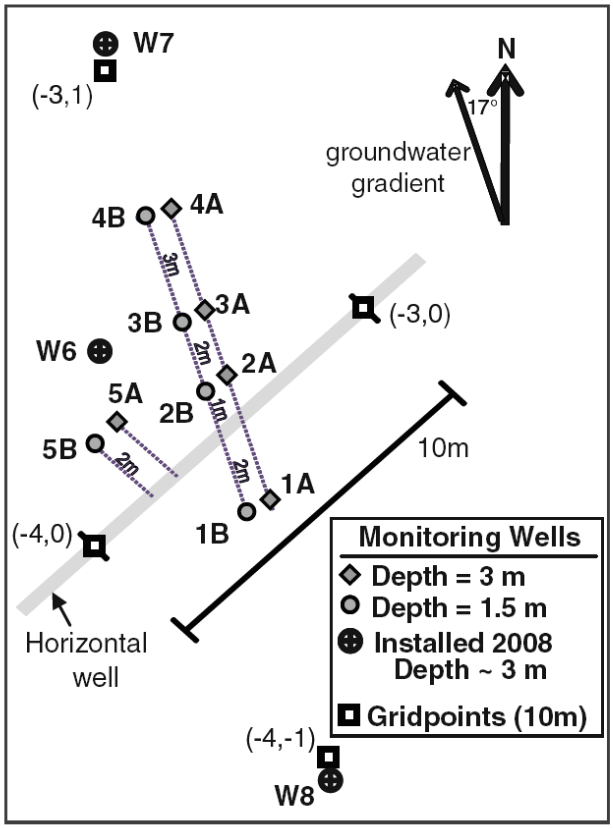

Figure 2. Plan view showing location of groundwater monitoring wells in relation to the surface trace of the slotted horizontal CO_2 injection pipe in zone 6 of the ZERT site (Kharaka et al., 2010). Note that further investigations since the start of this study point to a hydraulic gradient direction varying to the NNE.

Figure 3. Typical sediments at the test site consisting of a thin unsaturated layer of mostly sandy silt with grass roots (left), underlain by a thicker saturated layer of coarse sand, gravel and cobbles (right).

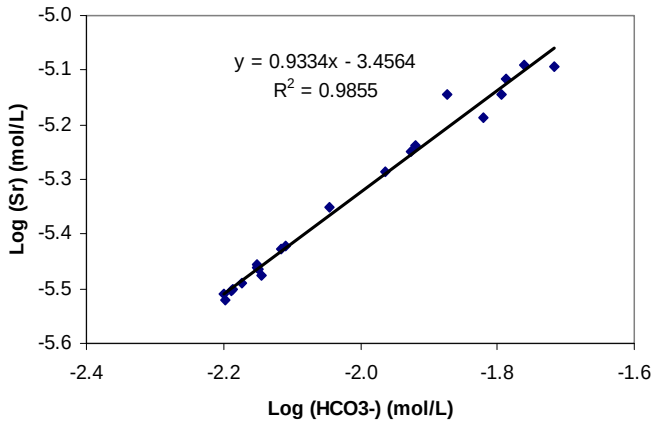

Figure 4. Correlation plots showing relationships between Sr and HCO_3^-.

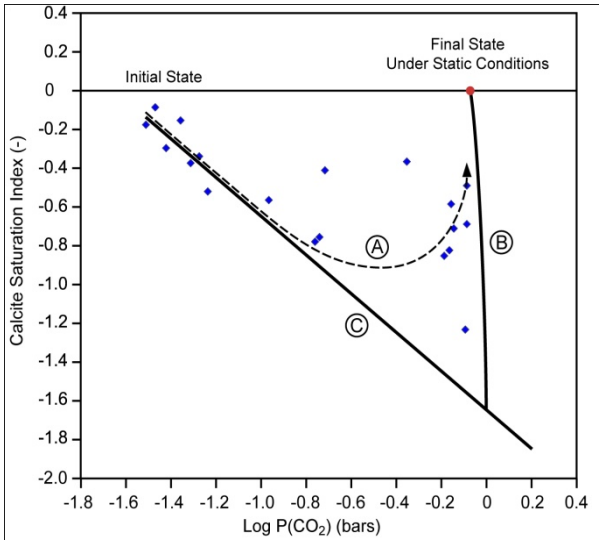

Figure 5. Saturation index of calcite as a function of log $P(CO_2)$ calculated for groundwater samples taken between July 7 and July 17, 2008 at the ZERT site. For an explanation of the trend lines, please refer to Section 4.3.

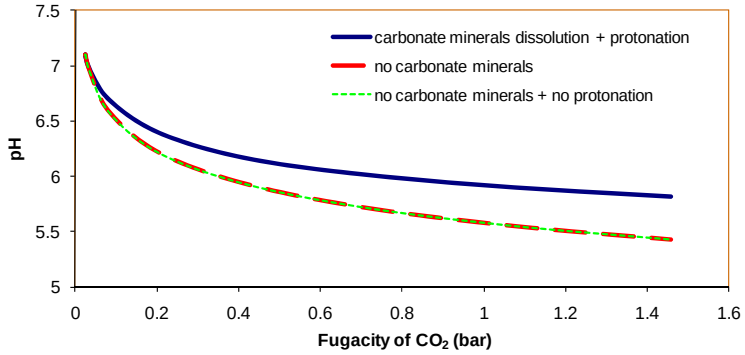

Figure 6. Calculated pH with different combination of chemical reactions

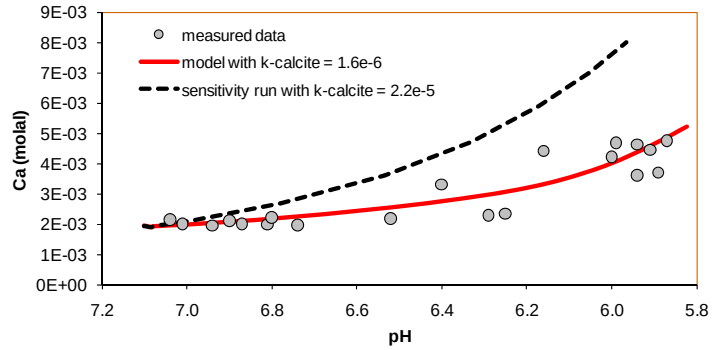

Figure 7. Calculated Ca concentration vs pH with different calcite dissolution rates (in mol/m^2/s) (Model B; Models A and C yield similar results).

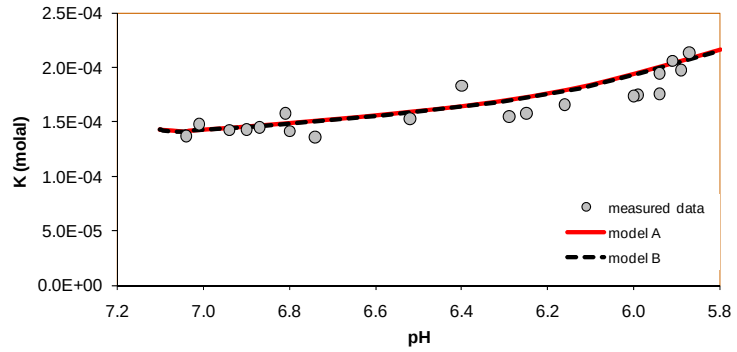

Figure 8. Calculated K concentration vs pH (Models A and B; Model C yields results similar to Model B).

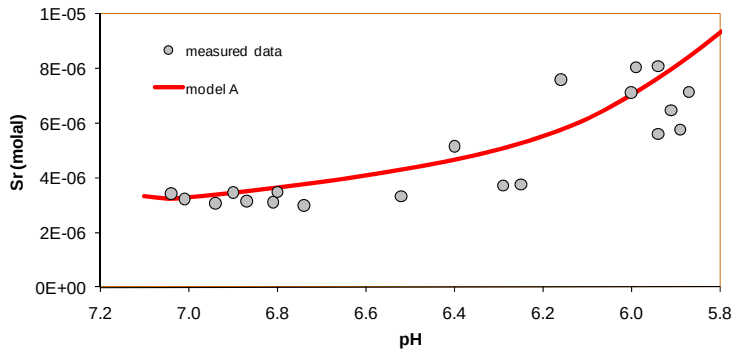

Figure 9. Calculated Sr concentration vs pH (Models A; Models B and C yield results similar to Model A).

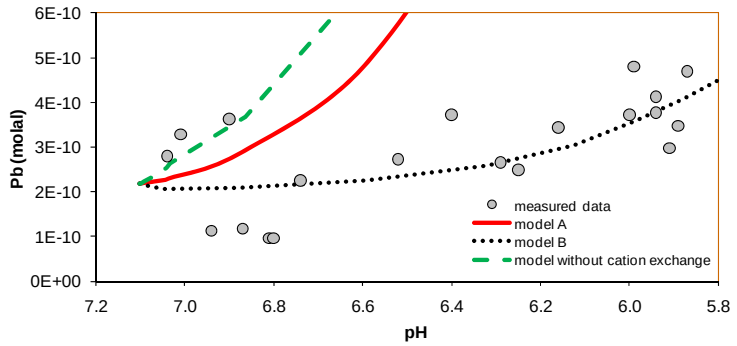

Figure 10. Calculated Pb concentration vs pH (Models A and B; Model C yields results similar to Model B).

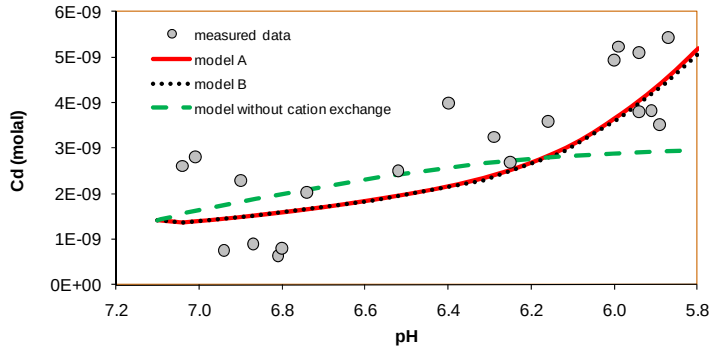

Figure 11. Calculated Cd concentration vs pH (Models A and B; Model C yields the same results as Model B).

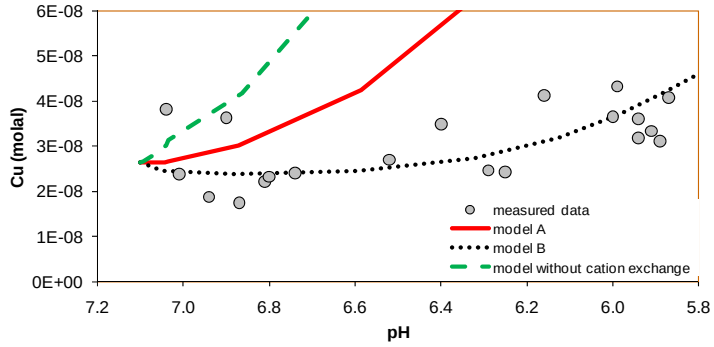

Figure 12. Calculated Cu concentration vs pH (Models A and B; Model C yields results similar to Model B).

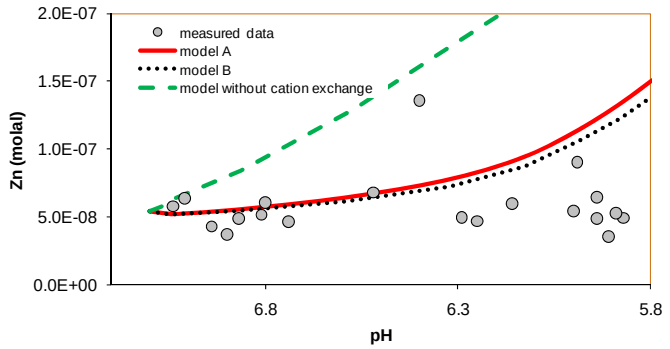

Figure 13. Calculated Zn concentration vs pH (Models A and B; Model C yields results similar to Model B).

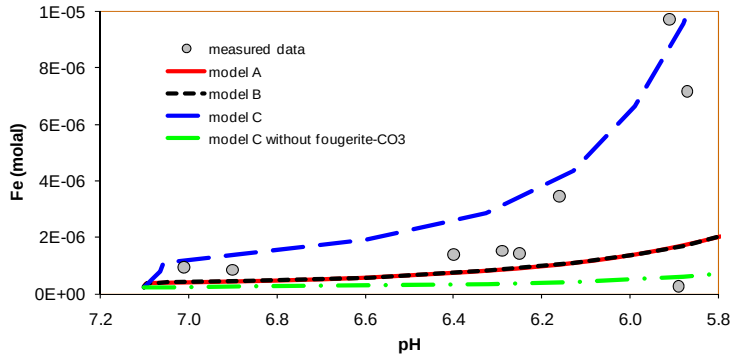

Figure 14. Calculated Fe concentration vs pH for various modeled scenarios.

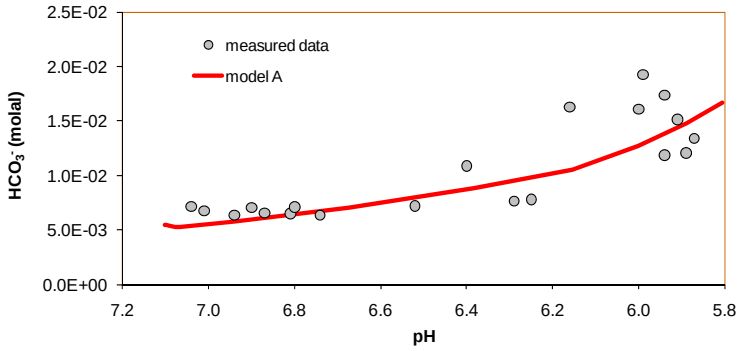

Figure 15. Predicted HCO_3^- concentration vs pH (Model A; Models B and C yields similar results).

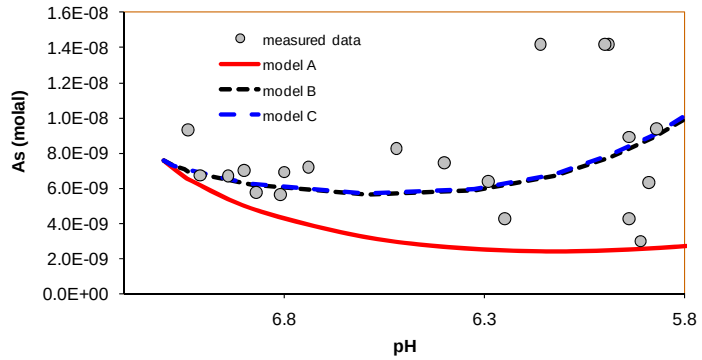

Figure 16. Predicted As concentration vs pH

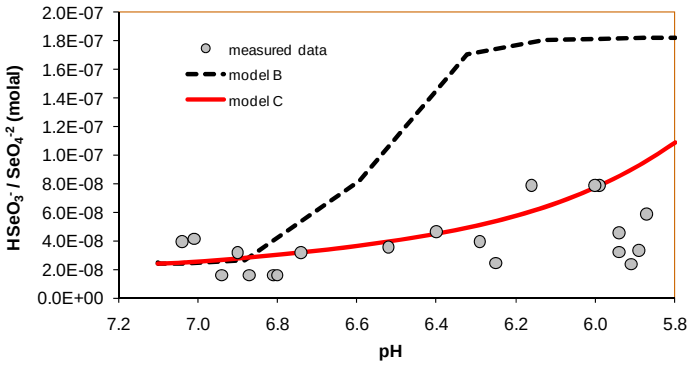

Figure 17. Predicted Se concentration vs pH (Models B and C; Model A yields results similar to Model B)

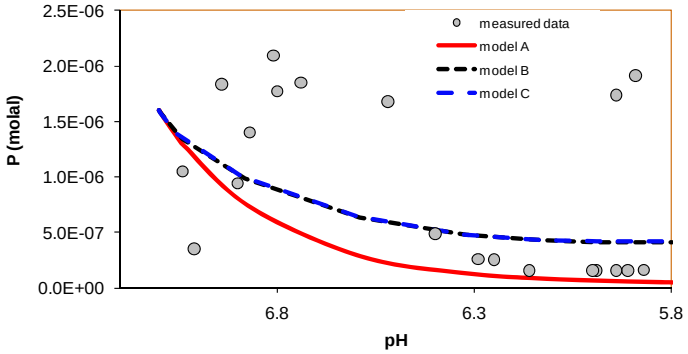

Figure 18. Predicted PO_4^{-3} concentration vs pH

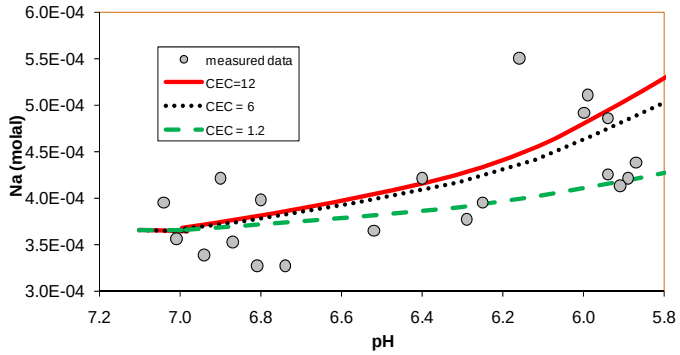

Figure 19. Sensitivity of Na concentration to CEC (meq/100 g)values (Model B with sorption disabled).

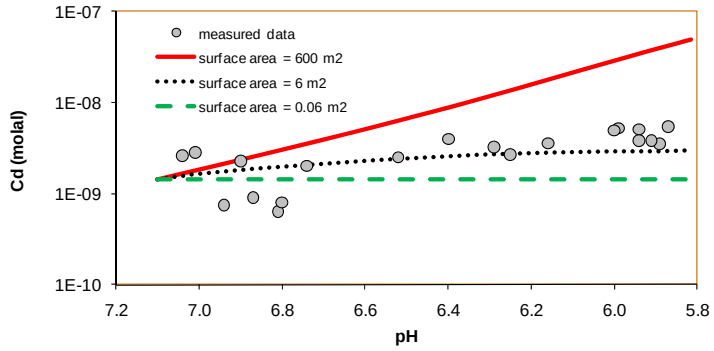

Figure 20. Sensitivity of Cd concentration to surface area (m^2/g) (Model A with exchange turned off).

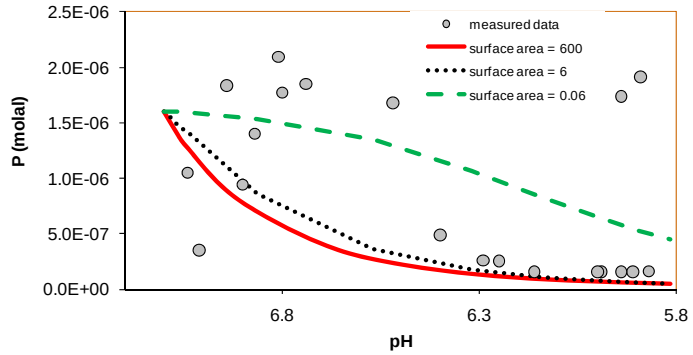

Figure 21. Sensitivity of PO_4^{-3} concentration to surface area (m^2/g) (Model A with exchange turned off).

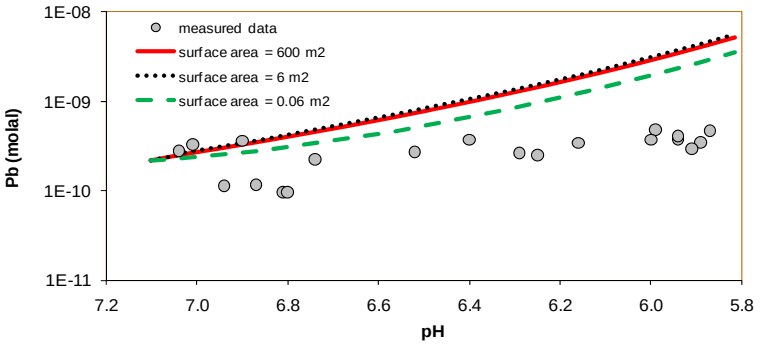

Figure 22. Sensitivity of Pb concentration to surface area (m^2/g) (Model A with exchange turned off).

Appendix A

The following rate equation was implemented (Lasaga et al., 1994; Steefel and Lasaga, 1994), including a pH dependency (Palandri and Kharaka, 2004) implemented as optional "acid" and "base" mechanisms in addition to the default "neutral" mechanism :

$$r = \pm k\ A\left[1-(Q/K)^{\theta}\right]^{\eta} \tag{1}$$

with

$$k = k_{25}^{nu}\exp\left[\frac{-E_a^{nu}}{R}\left(\frac{1}{T}-\frac{1}{298.15}\right)\right] + k_{25}^{H}\exp\left[\frac{-E_a^{H}}{R}\left(\frac{1}{T}-\frac{1}{298.15}\right)\right]a_H^{n_H} + k_{25}^{OH}\exp\left[\frac{-E_a^{OH}}{R}\left(\frac{1}{T}-\frac{1}{298.15}\right)\right]a_{OH}^{n_{OH}}$$

where r is the kinetic rate (positive values indicate dissolution, negative values precipitation), k is the rate constant (moles per unit mineral surface area and unit time), which is temperature dependent, A is the specific reactive surface area per kg H_2O, K is the equilibrium constant for the mineral–water reaction, and Q is the reaction quotient. Superscripts *nu*, *H*, and *OH* stand for the neutral, acid, and base mechanisms, E_a is activation energy, T absolute temperature, and a_H^n the hydrogen ion activity to some power n. Here, the parameters θ and η are assumed equal to unity. Rate constants, except for calcite (from Kaufmann and Dreybrodt, 2007) and a calibrated constant for fougerite (see main part of the paper), were taken from Xu et al. (2006), who used values mostly from Palandri and Kharaka (2004). For most minerals, surface areas are order-of-magnitude geometric estimates, assuming sub-mm-sized grains for clay minerals and mm-sized grains for other minerals. The surface area for calcite was taken from Anderson (1968); for fougerite, it was calibrated. Using these data, only calcite and fougerite are predicted to react to an extent sufficient to affect model results. Other minerals are predicted to be essentially unreactive over the relatively short simulated test period. Note that the surface area of ferrihydrite assumed for sorption (0.06, 6, and 600 m2/g, see main text) is much larger than that

assumed for precipitation or dissolution (Table A-1) and remains essentially constant in simulations because the adopted slow ferrihydrite reaction rate precludes significant dissolution of this mineral.

Table A-1. Initial volume fraction and kinetic parameters for minerals considered in the model (see text for source).

Mineral	**Volume fraction**	**A (cm^2/g) (for precipitation and dissolution)**	**Parameters for Kinetic Rate Law**							
			Neutral Mechanism		**Acid Mechanism**			**Base Mechanism**		
			k_{25} ($mol/m^2/s$)	**E_a (KJ /mol)**	**k_{25}**	**E_a**	**$n(H^+)$**	**k_{25}**	**E_a**	**$n(H^+)$**
Primary										
Quartz	0.35	9.8	1.023×10^{-14}	87.7						
Imogolite	0.05	9.8	1.023×10^{-14}	87.7						
Crandallite	0.05	9.8	1.023×10^{-14}	87.7						
K-feldspar	0.1	9.8	3.89×10^{-13}	38	8.71×10^{-11}	51.7	0.5	6.31×10^{-12}	94.1	-0.823
Oligoclase	0.318	9.8	1.44×10^{-12}	69.8	2.13×10^{-10}	65	0.457			
Smectite-Ca	0.01	151.6	1.66×10^{-13}	35	1.05×10^{-11}	23.6	0.34	3.02×10^{-17}	58.9	-0.4
Kaolinite	0.01	151.6	6.91×10^{-14}	22.2	4.89×10^{-12}	65.9	0.777	8.91×10^{-18}	17.9	-0.472
Illite	0.01	151.6	1.66×10^{-13}	35	1.05×10^{-11}	23.6	0.34	3.02×10^{-17}	58.9	-0.4
Ferrihydrite	0.01	12.9	2.52×10^{-12}	62.76	2.34×10^{-7}	43.54	1			
Magnetite	0.02	12.9	4.57×10^{-10}	23.5	4.17×10^{-7}	14.4	1			
Goethite	0.001	12.9	2.52×10^{-12}	62.76						
Calcite	0.05	3.05	1.6×10^{-6}	62.76						
Dolomite	0.02	12.9	2.52×10^{-12}	62.76	2.34×10^{-7}	43.54	1			
Fougerite	0.001	12.9	2.52×10^{-12}	62.76						
Secondary										
Magnesite		9.8	4.57×10^{-10}	23.5	4.17×10^{-7}	14.4	9.8			
Ankerite		9.8	1.26×10^{-9}	62.76	6.46×10^{-4}	36.1	0.5			
Dawsonite		9.8	1.26×10^{-9}	62.76	6.46×10^{-4}	36.1	0.5			
Pyromorphite		12.9	2.52×10^{-12}	62.76	2.34×10^{-7}	43.54	1			

Appendix B

Table B1 lists aqueous complexes included in the simulation and their dissociation constants, which are based on a database described in Wolery and Jove-Colon (2007). Table B2 lists the cation exchange reactions and their selectivity coefficients. The Gaines-Thomas convention is used here. The selectivity coefficients of the exchangeable cations except H^+ are taken from Appelo and Postma (1994). Most published selectivity coefficients for exchangeable H^+ are around 1 (e.g. Charlet and Tournassat, 2005; Tournassat et al., 2004; Sposito, et al., 1983), as listed in Table B2. The same selectivity coefficient for H^+ was also used in a model for the Hanford site (Zheng et al., 2008) which has similar mineralogical composition to the sediment at ZERT. Table B3 lists the surface complexation reactions. Surface complexation constants are taken from Dzombak and Morel (1990). Table B4 lists the log(K) of minerals when written in terms of the species listed in Table 2. These equilibrium constants were taken from the database described in Wolery and Jove-Colon (2007).

Table B1. Aqueous complexes and their dissociation constants.

Species	Logk (25°C)	Species	Logk (25°C)	Species	Logk (25°C)	Species	Logk (25°C)
OH^-	13.991	$Al(OH)_2^+$	-12.78	$Cu(CO_3)_2^{-2}$	10.476	$SrOH^+$	13.292
$CaHCO_3^+$	-1.043	$AlOH^{+2}$	-17.868	$NaHCO_3$(aq)	-0.17	$UO_2(CO_3)_2^{-2}$	3.747
$FeHCO_3^+$	-2.044	$Al_{13}O_4(OH)_{24}^{+7}$	-198.749	$NaSO_4^-$	-0.811	$UO_2(CO_3)_3^{-4}$	9.43
$FeCO_3$(aq)	4.879	$CdCl^+$	-1.966	NaCl(aq)	0.782	$UO_2(CO_3)$ (aq)	0.663
CO_2(aq)	-6.342	$HCOO_2^-$	21.243	$PbCl^+$	-1.456	$UO_2(OH)_2$(aq)	10.315
CO_3^{-2}	10.325	$HAsO_4^{-2}$	6.754	$PbCl_2$(aq)	-2.016	$Cr(OH)_3$(aq)	8.3
$MgHCO_3^+$	-1.033	$MnCO_3$(aq)	5.809	$SrSO_4$(aq)	-2.271	$Cr(OH)^{+2}$	-5.7
$MgSO_4$(aq)	-2.382	$MnHCO_3^+$	-0.882	$SrCO_3$(aq)	7.47	$CaHPO_4$(aq)	-2.69
$CaSO_4$(aq)	-2.1	$BaCO_3$(aq)	7.691	$SrCl^+$	0.253	$MgHPO_4$(aq)	-2.91
$HAlO_2$(aq)	-6.448	$CuOH^+$	7.287	$SrNO_3^+$	-0.796		

Table B2. Cation exchange reactions and selectivity coefficients.

Cation exchange reaction	$K_{Na/M}$
$Na^{+} + X\text{-}H = X\text{-}Na + H^{+}$	1
$Na^{+} + X\text{-}K = X\text{-}Na + K^{+}$	0.2
$Na^{+} + 0.5X\text{-}Ca = X\text{-}Na + 0.5Ca^{+2}$	0.4
$Na^{+} + 0.5X\text{-}Mg = X\text{-}Na + 0.5Mg^{+2}$	0.45
$Na^{+} + 0.5X\text{-}Pb = X\text{-}Na + 0.5Pb^{+2}$	0.4
$Na^{+} + 0.5X\text{-}Ba = X\text{-}Na + 0.5Ba^{+2}$	0.35
$Na^{+} + 0.5X\text{-}Cd = X\text{-}Na + 0.5Cd^{+2}$	0.4
$Na^{+} + 0.5X\text{-}Co = X\text{-}Na + 0.5Co^{+2}$	0.6
$Na^{+} + 0.5X\text{-}Cu = X\text{-}Na + 0.5Cu^{+2}$	0.5
$Na^{+} + 0.5X\text{-}Mn = X\text{-}Na + 0.5Mn^{+2}$	0.55
$Na^{+} + 0.5X\text{-}Sr = X\text{-}Na + 0.5Sr^{+2}$	0.35
$Na^{+} + 0.5X\text{-}Zn = X\text{-}Na + 0.5Zn^{+2}$	0.4
$Na^{+} + 0.5X\text{-}Fe = X\text{-}Na + 0.5Fe^{+2}$	0.6

Table B3. Surface complexation reactions and surface complexation constants (logK) on HFO.

Surface complexation	logK
$HFO\_sOH_2^+ = HFO\_sOH + H^+$	-7.29
$HFO\_wOH_2^+ = HFO\_wOH + H^+$	-7.29
$HFO\_sO^- + H^+ = HFO\_sOH$	8.93
$HFO\_wO^- + H^+ = HFO\_wOH$	8.93
$HFO\_sOHBa^{+2} = HFO\_sOH + Ba^{+2}$	-5.46
$HFO\_wOBa^+ + H^+ = HFO\_wOH + Ba_{+2}$	7.2
$HFO\_sOHCa^{+2} = HFO\_sOH + Ca^{+2}$	-4.97
$HFO\_wOCa^+ + H^+ = HFO\_wOH + Ca^{+2}$	5.85
$HFO\_wOMg^+ + H^+ = HFO\_wOH + Mg^{+2}$	4.6
$HFO\_sOCd^+ + H_+ = HFO\_sOH + Cd^{+2}$	-0.47
$HFO\_wOCd^+ + H^+ = HFO\_wOH + Cd^{+2}$	2.91
$HFO\_sOHSr^{+2} = HFO\_sOH + Sr^{+2}$	-5.01
$HFO\_wOSr^+ + H^+ = HFO\_wOH + Sr^{+2}$	6.58
$HFO\_sOPb^+ + H_+ = HFO\_sOH + Pb^{+2}$	-4.65
$HFO\_wOPb^+ + H^+ = HFO\_wOH + Pb^{+2}$	-0.3
$HFO\_sOCo^+ + H_+ = HFO\_sOH + Co^{+2}$	0.46
$HFO\_wO\ Co^{+2} + H^+ = HFO\_wOH + Co^{+2}$	3.01
$HFO\_sOCu^+ + H_+ = HFO\_sOH + Cu^{+2}$	-2.426
$HFO\_wOCu^{+2} + H^+ = HFO\_wOH + Cu^{+2}$	-0.137
$HFO\_sOZn^+ + H_+ = HFO\_sOH + Zn^{+2}$	-0.99
$HFO\_wOZn^{+2} + H^+ = HFO\_wOH + Zn^{+2}$	1.99
$HFO\_sOFe^+ + H_+ = HFO\_sOH + Fe^{+2}$	0.95
$HFO\_wOFe^{+2} + H^+ = HFO\_wOH + Fe^{+2}$	2.98
$HFO\_sOHSO_4^{-2} = HFO\_sOH + SO_4^{-2}$	-0.79
$HFO\_wOHSO_4^{-2} = HFO\_wOH + SO_4^{-2}$	-0.79
$HFO\_sSO_4^- + H_2O = HFO\_sOH + SO_4^{-2} + H^+$	-7.78
$HFO\_wSO_4^- + H_2O = HFO\_sOH + SO_4^{-2} + H^+$	-7.78
$HFO\_sSeO_4^- + H_2O = HFO\_sOH + H^+ + SeO_4^-$	-7.73
$HFO\_wSeO_4^- + H_2O = HFO\_wOH + H^+ + SeO_4^-$	-7.73
$HFO\_sMoO_4^- + H_2O = HFO\_sOH + MoO_4^- + H^+$	-9.5
$HFO\_wMoO_4^- + H_2O = HFO\_wOH + MoO_4^- + H^+$	-9.5
$HFO\_sOHMoO_4^{-2} = HFO\_sOH + MoO_4^{-2}$	-2.4
$HFO\_wOHMoO_4^{-2} = HFO\_wOH + MoO_4^{-2}$	-2.4
$HFO\_sH_2AsO_4 + H_2O = HFO\_sOH + H_2AsO_4^- + H^+$	-10.17
$HFO\_wH_2AsO_4 + H_2O = HFO\_wOH + H_2AsO_4^- + H^+$	-10.17

$HFO\_sHAsO_4^- + H_2O = HFO\_sOH + H_2AsO_4^-$	0.35
$HFO\_wHAsO_4^- + H_2O = HFO\_wOH + H_2AsO_4^-$	0.35
$HFO\_sH_2PO_4 + H_2O = HFO\_sOH + HPO_4^{-2} + 2H^+$	-18.9
$HFO\_w\ H_2PO_4 + H_2O = HFO\_wOH + HPO_4^{-2} + 2H^+$	-18.9
$HFO\_sPO_4^{-2} + H_2O = HFO\_sOH + HPO_4^{-2}$	-5.4
$HFO\_wPO_4^{-2} + H_2O = HFO\_wOH + HPO_4^{-2}$	-5.4
$HFO\_wCO_2^- + H_2O = HFO\_sOH + HCO_3^-$	-2.45
$HFO\_wCO_2H + H_2O = HFO\_sOH + HCO_3^- + H^+$	-10.4

Table B4. Equilibrium constants for minerals

Primary Mineral	log(*K*)	Primary Mineral	log(*K*)
Quartz	-3.75	Illite	-47.42
Imogolite	-31.75	Ferrihydrite	-63.24
Crandallite	-76.07	Magnetite	-6.505
K-feldspar	-22.91	Goethite	-8.12
Oligoclase	-97.78	Calcite	1.85
Smectite-ca	-39.51	Dolomite	2.524
Kaolinite	-39.9	Fougerite	24.24
Magnesite	2.299	Ankerite	-1.035
Dawsonite	-18.532	Pyromorphite	-48.015